Title

Implementation and Characterization of a Novel Solid-State Refrigerator Based on the Electrocaloric Effect and Liquid-Based Switchable Thermal Interfaces

Author

Jia, Yanbing

Publication Date

2014

Peer reviewed|Thesis/dissertation

UNIVERSITY OF CALIFORNIA

Los Angeles

Implementation and Characterization of a Novel Solid-State Refrigerator Based on the Electrocaloric Effect and Liquid-Based Switchable Thermal Interfaces

A dissertation submitted in partial satisfaction

of the requirements for the degree

Doctor of Philosophy in Mechanical Engineering

by

Yanbing Jia

2014

ABSTRACT OF THE DISSERTATION

Implementation and Characterization of a Novel Solid-State Refrigerator Based on the Electrocaloric Effect and Liquid-Based Switchable Thermal Interfaces

by

Yanbing Jia

Doctor of Philosophy in Mechanical Engineering

University of California, Los Angeles, 2014

Professor Yongho Sungtaek Ju, Chair

As an intriguing alternative to the Peltier effect, the electrocaloric (EC) effect refers to changes in the temperature of a material when an external electric field is applied to and removed from the material. Since the EC effect is a reversible phenomenon, the efficiency of EC cooling can closely approach the Carnot limit. Despite its great potential, technical challenges remain to realize practical coolers based on this giant EC effect. The ΔT achievable in bulk materials is typically small and high ΔT can only be achieved so far in thin films of both ceramics and polymers. Due to their small thermal masses, thin film EC materials must undergo thermodynamic cycles at relatively high frequencies to

achieve high cooling power densities per unit area. However, high frequency operations may also lead to significant losses, which in turn pose more stringent limits on the acceptable on/off ratio as well as the off-state thermal resistance of thermal switches. In addition, innovative structures need to be designed to compensate for the small thermal masses by stacking multiple EC thin-films together while avoiding temperature non-uniformity due to the low thermal conductivity of typical EC materials.

In the present work, we first design a switchable thermal interface based on an array of discrete liquid droplets initially confined on hydrophilic islands on a substrate. The rupture distance, loading pressure, thermal resistance in the on-state and the reliability of the interface are evaluated both theoretically and experimentally to find the optimal design for practical applications.

We also present a solid-liquid hybrid thermal interface for reliable low-contact pressure (< 1 kPa) switching with on-state thermal contact resistance < 15 $x10^{-6}$ m^2K/W. Reduction in the thermal resistance of hybrid interfaces created through electroplating is evaluated using transient pulsed heating measurements and thermal time constant characterization.

We then demonstrate our new device concept of a compact solid-state cooling module based on the giant electrocaloric effect. Our novel design realizes controllable thermodynamic cycles for the ferroelectric material thin films with laterally interdigitated electrodes. It also exploits the liquid-based thermal interfaces to enable reliable and high-contrast thermal switching and at the same time offer high off-state resistance to

minimize deleterious parasitic heat transfer. We numerically simulate the cooling performance, as well as experimentally confirm ~1 K temperature drop at the operation frequency of ~0.3 Hz.

Since the performance of the current EC cooling device is limited by the material intrinsic properties, we design two methods to characterize the EC effect so that we can find the optimal material for high performance solid-state EC refrigerator. One is a direct thermal characterization of the electrocaloric (EC) heating and cooling in thin films supported on substrates using microfabricated thin-film resistance thermometers. We analyze the temporal temperature profiles through full three-dimensional heat diffusion modeling to obtain effective adiabatic temperature changes.

The other is a direct characterization of the frequency dependent temperature responses in EC thin films under AC bias electric fields using a high-precision lock-in technique. The temperature responses detected by embedded thin-film resistance thermometers are analyzed using the steady periodic solutions of the 3D heat conduction model to extract the equivalent volumetric heat sources, corresponding respectively to the electrocaloric effects and hysteresis losses.

The dissertation of Yanbing Jia is approved.

Adrienne Lavine

Chang-Jin Kim

Bruce S. Dunn

Yongho Sungtaek Ju, Committee Chair

University of California, Los Angeles

2014

TABLE OF CONTENTS

LIST OF FIGURES

ACKNOWLEDGEMENTS

This work would not have been possible without the support of many people. I would like to first express my sincere gratitude to my advisor, Professor Y. Sungtaek Ju, for his enthusiastic guidance and insightful advises throughout my PhD research. I would also like to thank the committee members, Professors B. Dunn, A. Lavine, and C-J Kim, for their valuable suggestions and encouragement.

I am indebted to former and current colleagues in UCLA Multiscale Thermosciences Laboratory: Youngsuk Nam, Gillwan Cha, Tanye Tang, Katie Bulgrin, Stephen Sharratt, Yujia Zhan, Jingda Zhuang, Cheng Peng, and Yang Shen. I am especially grateful to Gillwan Cha for his help. I am also thankful to my friends: Wenying Gan, Anqi Yang, and Tianyu Wu for their support during my stay at UCLA.

Last but not least, I would like to thank my family and friends for their love, encouragement and continued support over the years. My deepest gratitude goes to my parents for their unconditional love and support.

VITA

2010	B.S., Electrical Engineering Peking University Beijing, China
2010-2014	Graduate Student Researcher/Teaching Assistant Mechanical and Aerospace Engineering Department University of California, Los Angeles

PUBLICATIONS

Journal Publications

Jia, Y., and Ju, Y. S., "Solid-liquid hybrid thermal interfaces for low-contact pressure thermal switching," Journal of Heat Transfer, Vol. 136, 2014, 074503

Jia, Y., and Ju, Y. S., "Direct characterization of the electrocaloric effects in thin films supported on substrates," Applied Physics Letters, Vol. 103, 2013, 042903

Jia, Y., and Ju, Y. S., "A solid-state refrigerator based on the electrocaloric effect," Applied Physics Letters, Vol. 100, 2012, 242901

Jia, Y., Cha, G., and Ju, Y. S., "Switchable thermal interfaces based on discrete liquid droplets," Micromachines, Vol. 3, 2012, pp. 10–20

Conference Proceedings and Presentations

Jia, Y., and Ju, Y. S., "Solid-liquid hybrid thermal interfaces for low-contact pressure thermal switching", Presented in 2013 ASME International Mechanical Engineering Congress & Exposition, November 15-21, 2013, San Diego, California, USA

Jia, Y., and Ju, Y. S., "Solid-state refrigerator based on the Electrocaloric effect", Presented in 2012 ASME International Mechanical Engineering Congress & Exposition, November 9-15, 2012, Houston, Texas, USA

Cha, G., **Jia, Y.**, and Ju, Y. S., "High-power density pyroelectric energy harvesters incorporating switchable liquid-based thermal interfaces", In Proceedings of IEEE Conference MEMS 2012, January 29 – February 2, 2012, Paris, France

CHAPTER 1

Introduction

1.1 Switchable Thermal Interfaces

1.1.1 Switchable Thermal Interfaces for Low-Power Thermal Control and Thermal Management

Switchable thermal interfaces enable controlled modulation of thermal conductance between devices of interest and their heat sinks/sources. They are key components of micro-devices and systems that require reconfigurable heat transfer paths for precise low-power thermal control and management. Potential applications include micro-bolometers with locally adjustable dynamic ranges, electrostatic switched radiators, chip scale atomic clocks with low-power precision temperature controls, pulsed thermoelectric cooling, solid-state electrocaloric refrigerators that require rapid thermal cycling of the working medium, pyroelectric waste heat harvesting, and satellite thermal management [1-8].

Figure 1.1 shows the schematic of the thermoelectric cooler with thermal switches. The performance of thermoelectric coolers is enhanced by applying high-amplitude transient electrical pulses to the thermoelectric elements [9]. However, the Joule heating produced in the bulk elements during the pulse diffuses towards both junctions of the device. The thermal switch between the thermoelectric elements and the object to be cooled can break the thermal contact before the cooling is degraded by the excess flow of Joule heat.

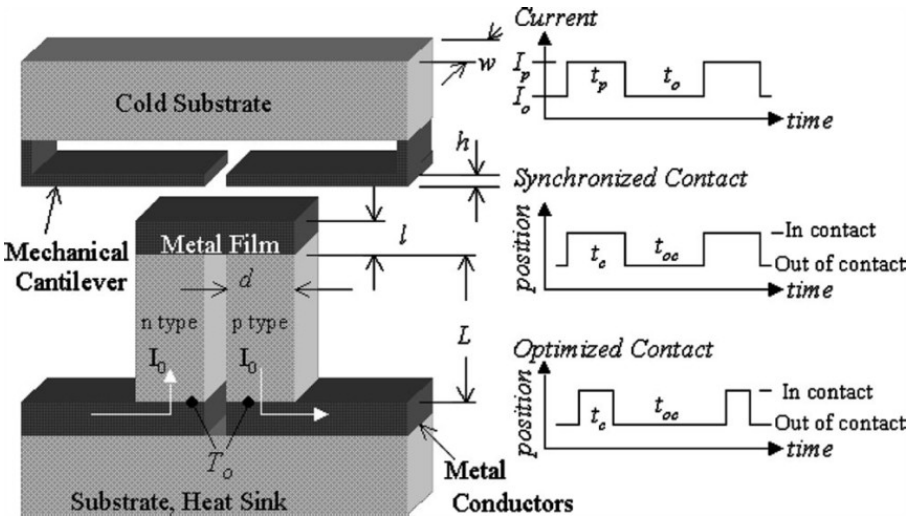

Figure 1.1: Schematic diagram of the thermoelectric cooler with thermal switches. The diagram shows the optimized contact, for which pulse width (t_p) is longer than contact time (t_c). Contact time (t_c) of optimized operation is designed such that heat flow is only from the cantilever to the cold junction. [9]

Another example is the application of switchable thermal interfaces in a pyroelectric energy harvester, as shown in Figure 1.2. In the non-conducting or off state, the

pyroelectric material is physically separated from the hot (cold) surface by air. In the conducting or on state, the pyroelectric material is pressed against the hot (cold) surface to deform the liquid droplets into a continuous thin layer with low thermal resistance. [10]

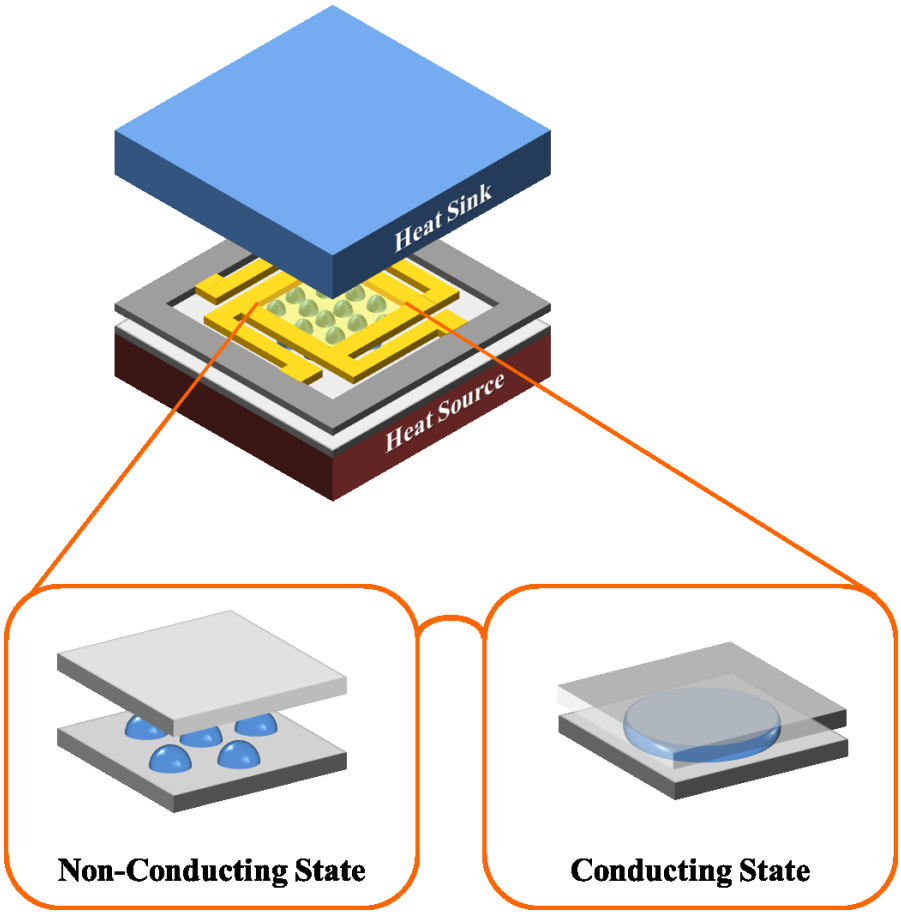

Figure 1.2: Schematic of the micro-pyroelectric power generator module. The pyroelectric thin film assembly is actuated up and down to make alternating thermal contacts with the cold side and the hot side via switchable thermal interfaces. [10]

1.1.2 Drawbacks of Solid-Solid Contact Based Thermal Interfaces

It is well-established that thermal transport across solid-solid contacts is often limited by surface asperities that reduce actual contact areas. Previous experimental studies showed, however, that significant loading pressure (in the order of 1 MPa) is necessary to achieve small thermal contact resistance ($<10^{-4}$ m^2•K•W) even for micromachined silicon surfaces with nanometer scale roughness [1]. This may be attributed to trapped gas layers that strongly impede heat conduction.

Dense arrays of vertically aligned carbon nanotubes [11] or nanofibers [12] have received a lot of attention for potential heat transfer applications. Relatively large loading pressure was, however, often necessary to achieve small thermal resistance because only a small fraction of tubes actually make contact with the opposing surface. Furthermore, under intimate contacts, strong adhesion between carbon nanotubes and the opposing surface [13] and resulting delamination failures make them ill-suited as switchable thermal interfaces.

1.1.3 Liquid-Based Switchable Thermal Interfaces

Liquid-mediated thermal interfaces can make complete contacts and circumvent deleterious effects of gas layers trapped between the surfaces, which are also expected to be immune to fracture, cold-welding, and other failure mechanisms that may limit practical applications of direct solid-solid contacts.

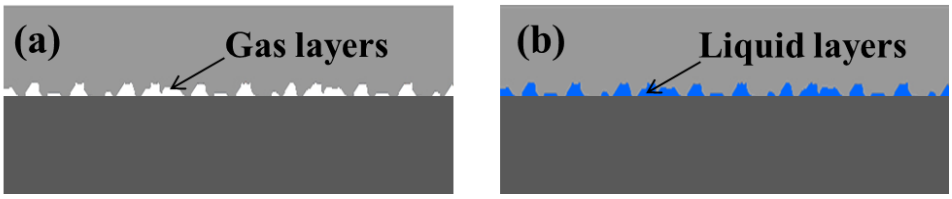

Figure 1.3: Solid-solid contact (a) with trapped gas layers and (b) mediated with liquid layers.

A previous study demonstrated a related thermal switch that consists of an array of discrete mercury droplets [2]. Since the thermal conductivity of mercury is relatively high, the thermal resistance across each droplet can be very low (~4×10^{-6} m^2•K•W). Mercury, however, poses health and environmental hazards. Some alternative room-temperature liquid metals can circumvent this issue, but they oxidize rapidly in the ambient air, making their practical use difficult.

A recent study demonstrated the potential for an alternative liquid-mediated thermal interface, which can provide thermal contact resistance comparable to that of direct solid-solid contacts at loading pressure several orders of magnitude smaller [14]. The key idea was to exploit the predominance of surface tension over gravity and other bulk forces at microscales to reversibly change the morphology of parallel columns of a dielectric liquid confined in microchannels.

In its off-state, the two surfaces defining the interface are separated from each other by an air or vacuum gap. The liquid is confined in an array of discrete microchannels separated from each other by hydrophobic regions. The two surfaces are then brought into contact to compress and deform the liquid columns until a continuous liquid layer is

formed. To switch off the interface, the two surfaces are pulled away from each other. The continuous liquid layer is then first transformed into an array of liquid bridges spanning the gap, which then rupture to break thermal contact between the two surfaces.

The channel-based liquid thermal interface has the advantages that it can be easily manufactured using standard microfabrication techniques and that each channel can readily be filled with a precise amount of liquid to control the final gap distance.

1.2 Electrocaloric Effect and Characterization Methods

The electrocaloric (EC) effects represent changes in the entropy and hence the thermal state of a polarizable material in response to a change in the applied electric field. A number of recent studies explored the electrocaloric effects in organic and inorganic materials, especially their thin films, with potential applications in solid-state refrigeration [15-18].

Figure 1.4 illustrates schematically the ECE in a dipolar material. Application of an electric field to the material causes partial alignment of dipoles and consequently a reduction of entropy of the dipolar system. In an adiabatic process, to keep the total entropy of the material constant, the temperature of the dielectric is increased by ΔT, the adiabatic temperature change. In a reverse process, as the applied electric field is reduced to zero and the dipoles return to the less ordered state (or disordered state), an increase in

the entropy of dipolar system occurs and the temperature decreases. [19]

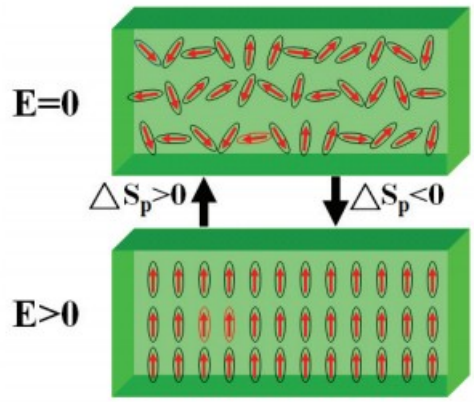

Figure 1.4: Schematic drawing of the ECE process in a dipolar material. When E=0, the dipoles orient randomly. When E>0, especially larger than the coercive electric field, the dipoles orient along the electric field direction. [19]

The large EC effects reported in thin films were often obtained using the "indirect method," which involves analysis of temperature-dependent polarization data under the general framework of the Maxwell relations, or using calorimetric measurements [20-21]. Direct measurement of the EC effects in thin films supported on a substrate is very challenging because the thermal mass of the films is much smaller than that of the substrate. Some previous studies used small-bead thermistors to measure the adiabatic temperature change in free-standing foils of polymeric materials or multi-layer capacitor structures [22-23]. Although experimental measurements of the adiabatic temperature

changes in thin ceramic films supported on substrates were reported in one previous study, no actual temporal temperature profiles obtained or detailed thermal analysis were reported to establish the validity and accuracy of the reported values.

A more recent study [24] used a scanning thermal microscopy probe and an infrared imager to directly measure the adiabatic temperature changes in multi-layer capacitor structures. Although the potential of applying such approaches directly to thin films prepared on substrates has been suggested, scanning thermal microscopy is not readily accessible to many research groups.

1.3 Solid-State EC Refrigerators

Peltier coolers are de facto standard solid-state refrigerators, where the refrigeration effect can be achieved without using any moving parts but by simply passing a small current through a closed circuit made up of two dissimilar materials, as shown in Figure 1.5. Major R&D programs over the past two decades have resulted in superlattices and so-called nano-bulk TE materials with figures of merit $ZT > 1$. However, direct demonstration of coolers with significantly enhanced performance has yet to be reported.

As an intriguing alternative to the Peltier effect, the electrocaloric (EC) effect refers to changes in the temperature of a material when an external electric field is applied to and removed from the material. Since the EC effect is a reversible phenomenon, the efficiency of EC cooling can closely approach the Carnot limit. Furthermore, electric

fields can be readily confined across small gaps, greatly facilitating the implementation of compact cooling modules based on the EC effect.

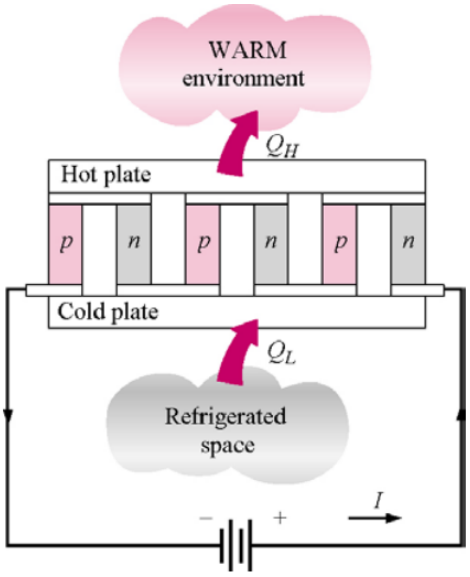

Figure 1.5: Device design of a thermoelectric refrigerator.

Despite its great potential, the EC effect has found very limited usage so far because the ΔT achievable in bulk materials is typically less than 2 K. A major breakthrough came when studies suggested that ΔT as high as 12 K can be achieved in thin films of both ceramics and polymers [25-26]. Technical challenges remain, however, to realize practical coolers based on this giant EC effect.

Early studies [27] used bi-directional pumps to circulate heat transfer fluids around bulk EC ceramics to achieve a continuous refrigeration cycle. The low operating frequency (and hence cooling power) and the poor efficiency and reliability of fluid pumps, however, have hampered their further development.

Due to their small thermal masses, thin film EC materials must undergo thermodynamic cycles at relatively high frequencies to achieve high cooling power densities per unit area. Recent studies reported conceptual designs for EC coolers based on thin films [16, 28-30]. For example, as shown in Figure 1.6, layers of electrocaloric material coupled with thin-film heat switches can work as either refrigerators and heat pumps or electrical generators, depending on the phasing of the applied voltages and heat switching. However, their physical implementation and experimental characterization have not been reported, and the validity of these design analyses needs to be carefully examined as they overlooked the impact of slow heat diffusion in EC materials and significant losses at high cycle frequencies.

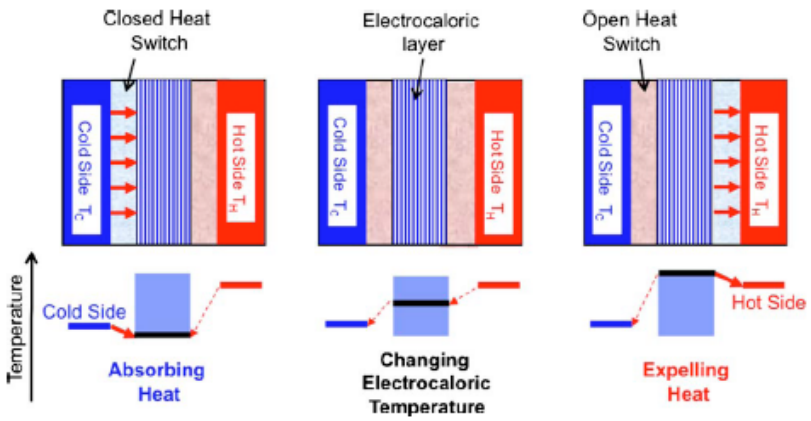

Figure 1.6: Schematic of a one-active-layer thin-film cooler. The top panels indicate the operation of the thermal switches during different intervals of the cooling cycle. The bottom panels show the temperature of the electrocaloric layer and the heat flows. The solid arrows show the preferred heat flows and the dashed show unwanted heat leakages. [30]

The previous design analyses assumed that the electric polarization and depolarization steps can occur instantaneously and that negligible "parasitic" heat transfer occurs during these steps. This led to a somewhat puzzling conclusion that an optimal cooling efficiency could be achieved using thermal switches with on/off resistance ratios of only about 6. In practice, ferroelectric materials suffer from significant hysteresis losses at high switching frequencies (of the order of 1 kHz and greater). The large drive currents necessary at high frequencies not only lead to significant losses but also raise concerns about the reliability of the drive circuitry. Due to these practical considerations,

the polarization/depolarization times must be finite, which in turn poses more stringent limits on the acceptable on/off ratio as well as the off-state thermal resistance of thermal switches.

To compensate for the small thermal masses of thin-films, one may stack multiple EC thin-films together. The low thermal conductivity of typical EC materials, however, leads to temperature non-uniformity across the stack, which in turn significantly degrades cooler performance. This limits the total thickness of EC materials one can use and, as a result, the minimum cycle frequency necessary to achieve a given cooling power density per unit area.

1.4 Scope of Research

The present work studies the characterization and optimization of liquid-based switchable thermal interfaces and solid-state EC refrigerators.

Chapter 2 presents a switchable thermal interface based on an array of discrete liquid droplets initially confined on hydrophilic islands on a substrate. We investigate a criterion for reversible switching in terms of hydrophilic pattern size and liquid volume. The dependence of the liquid morphology and rupture distance on the diameter and areal fraction of hydrophilic islands, liquid volumes, as well as loading pressure is also characterized both theoretically and experimentally.

Chapter 3 explores a solid-liquid hybrid thermal interface for reliable low-contact pressure (< 1 kPa) switching with on-state thermal contact resistance < 15 x10^{-6} m^2K/W. Reduction in the thermal resistance of hybrid interfaces created through electroplating was evaluated using transient pulsed heating measurements and thermal time constant characterization. Compared with pure liquid-mediated interfaces and direct solid-solid contacts reported previously, the hybrid interface shows superior thermal performance under the same loading pressure while avoiding the use of liquid metals.

Chapter 4 discusses a new device concept of a compact solid-state cooling module based on the giant electrocaloric effect. Our novel design realizes controllable thermodynamic cycles for the ferroelectric material thin films with laterally interdigitated electrodes. It also exploits the liquid-based thermal interfaces to enable reliable and high-contrast thermal switching and at the same time offer high off-state resistance to minimize deleterious parasitic heat transfer. We numerically simulate the cooling performance, as well as experimentally confirm ~1 K temperature drop at the operation frequency of ~0.3 Hz.

Chapter 5 presents a direct thermal characterization of the electrocaloric (EC) heating and cooling in thin films supported on substrates using microfabricated thin-film resistance thermometers. We analyzed the temporal temperature profiles through full three-dimensional heat diffusion modeling and compared results obtained using thin-film thermometers with different temperature coefficients of resistance to assess potential experimental error due to electric or electromagnetic coupling and thereby further validate our approach.

Chapter 6 presents a direct characterization of the frequency dependent temperature responses in EC thin films under AC bias electric fields using a high-precision lock-in technique. The temperature responses detected by embedded thin-film resistance thermometers are analyzed using the steady periodic solutions of a 3D heat conduction model to extract the equivalent volumetric heat sources, corresponding respectively to the electrocaloric effects and hysteresis losses. The bias filed frequency and amplitude dependence of the heat sources agrees well with our model predictions, and the volumetric heating rates due to the hysteresis losses are estimated to be as much as 15% of the EC heating/cooling rates for the EC material studied here.

CHAPTER 2

Switchable Thermal Interfaces Based on Discrete Liquid Droplets

In this chapter, we present a switchable thermal interface based on an array of discrete liquid droplets initially confined on hydrophilic islands on a substrate. The droplets undergo reversible morphological transition into a continuous liquid film when they are mechanically compressed by an opposing substrate to create low-thermal resistance heat conduction path. We investigate a criterion for reversible switching in terms of hydrophilic pattern size and liquid volume. The dependence of the liquid morphology and rupture distance on the diameter and areal fraction of hydrophilic islands, liquid volumes, as well as loading pressure is also characterized both theoretically and experimentally. The thermal resistance in the on-state is experimentally characterized for ionic liquids, which are promising for practical applications due to their negligible vapor

pressure. A life testing setup is constructed to evaluate the reliability of the interface under continued switching conditions at relatively high switching frequencies.

2.1 Background

As discussed in the first chapter, the main drawback of channel-based design of the liquid-based switchable thermal interface, however, has to do with its requirement for a long mechanical stroke. The distance required for liquid-bridges to rupture is in the order of the length of microchannels, which can be in the order of 1 mm. This can be problematic in applications that require micro-actuators of limited actuation ranges or small off-state gaps to achieve rapid thermal cycling.

The present work reports our theoretical and experimental work on an alternative design that replaces microchannels with an array of discrete chemically-patterned hydrophilic islands to reduce or otherwise control the liquid-bridge rupture distance. As an illustration, Figure 1 shows a difference in rupture distance between two patterns. For the same liquid volume, the rupture distance of the interface containing circular islands is below 300 μm [Figure 2.1(a)], whereas that of the interface containing parallel microchannels is over 700 μm [Figure 2.1(b)].

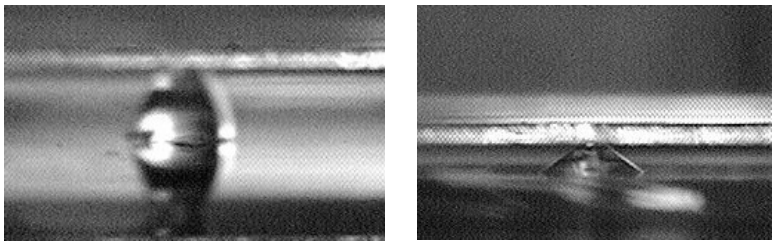

(a) **(b)**

Figure 2.1: Comparison between the rupture distances of (a) microchannel pattern and (b) discrete circular pattern.

2.2 Interface Design

2.2.1 Reversibility

One key design consideration for the switchable thermal interfaces is their reversibility. That is, a continuous liquid film formed by deforming and merging an array of discrete liquid droplets must be able to return to the original state of discrete droplets when the two surfaces are separated from each other.

We consider an array of circular hydrophilic patches on an otherwise hydrophobic surface as our model system. The two main design parameters are (1) pattern size d as characterized by their diameters and (2) the pattern areal fraction f, which is defined as the fraction of the surface area occupied by hydrophilic islands. When d or f is too small, a continuous liquid film formed in the switch-on state may transform into a single large

liquid drop instead of an array of multiple discrete droplets as illustrated in Figure 2.2(a,b).

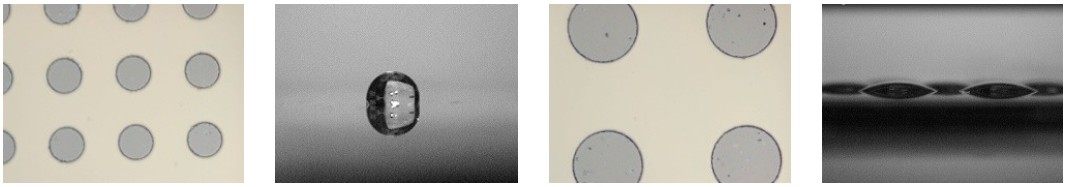

(a) **(b)** **(c)** **(d)**

Figure 2.2: Comparison between large and small patterns. Liquid will transform into a single droplet (b) on the substrate with small patterns (a) or stay as discrete droplets (d) on the substrate with large patterns (c).

To establish quantitative reversibility criteria, we compare the interface energies of the single-droplet state and the discrete multi-droplet states. Assuming that the effect of the gravity is negligible, we can approximate liquid droplets as truncated spheres. The interfacial energy can then be written as

$$E_s = \left[2\pi r^2 \frac{1-\cos\theta_2}{\sin^2\theta_2} - \cos\theta_1 \cdot \pi r^2 \cdot f - \cos\theta_2 \cdot \pi r^2 \cdot (1-f)\right] \cdot \gamma_{lv} \tag{2.1}$$

$$E_m = f\left[2\,\frac{1-\cos\alpha}{\sin^2\alpha} - \cos\theta_1\right] \cdot \gamma_{lv} \cdot \frac{V}{g} \tag{2.2}$$

$$V = \frac{\pi r^3}{3}\frac{(1-\cos\theta_2)^2}{\sin^3\theta_2}(2+\cos\theta_2) \tag{2.3}$$

Here r is the radius of the wetting area of the single droplet at the initial state, which is determined by the total volume (Eq. 2.3), α is the apparent contact angle of a discrete droplet on each hydrophilic pattern, g is the desired minimum gap (or the target minimum thickness of the continuous liquid layer), and V is the total liquid volume.

Figure 2.3 shows the calculated interfacial energy for the two states at $f = 0.2$, $V = 0.7$ μL and $g = 20$ μm. We consider a case where the contact angle on the hydrophilic pattern is $\theta_1 = 24.4°$ (experimentally measured for silicon after patterning) and that on the hydrophobic region (e.g., Teflon® coating) θ_2 is 120°. The liquid-vapor surface tension γ_{lv} = 73 mN/m is assumed to be comparable to that of water.

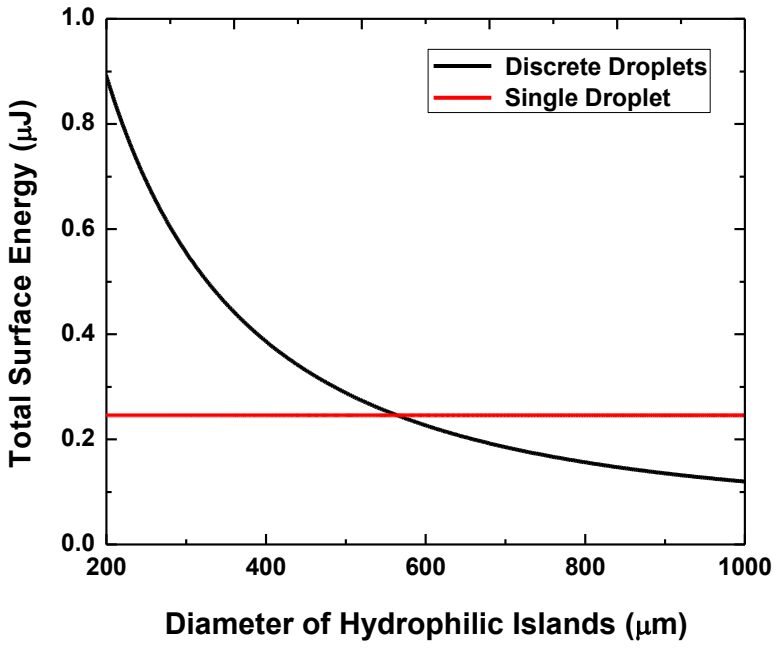

Figure 2.3: Interface energies of the single-droplet state and the multi-droplet states versus pattern size.

When the pattern size is below approximately 560 μm, the discrete multi-droplet state has higher energy and is hence less energetically favorable than the single-drop state. That is, a continuous liquid layer will more likely transform into a single large liquid drop when the two surfaces are separated from each other than to form multiple discrete droplets. The pattern size needs to exceed this value to achieve the reversibility.

Figure 2.4(a) shows the difference in the interfacial energy of the two states for different values of the pattern areal fraction *f*. The x-intercepts, ranging from approximately 500 to 700 μm, correspond to the minimum pattern size necessary for the discrete multi-drop state to be energetically more favorable. This minimum pattern size decreases with increasing *f*. In other words, smaller patterns can achieve reversibility at higher pattern fractions where the neighboring hydrophilic patterns are located closer to each other. When the pattern size becomes very large, the interfacial energy difference decreases with increasing pattern density. Liquid droplets on these large patterns are more prone to merge and form a single large drop. As shown in Figure 2.4(b), smaller apparent angles are necessary to prevent the coalescence of neighboring liquid drops at higher pattern fractions.

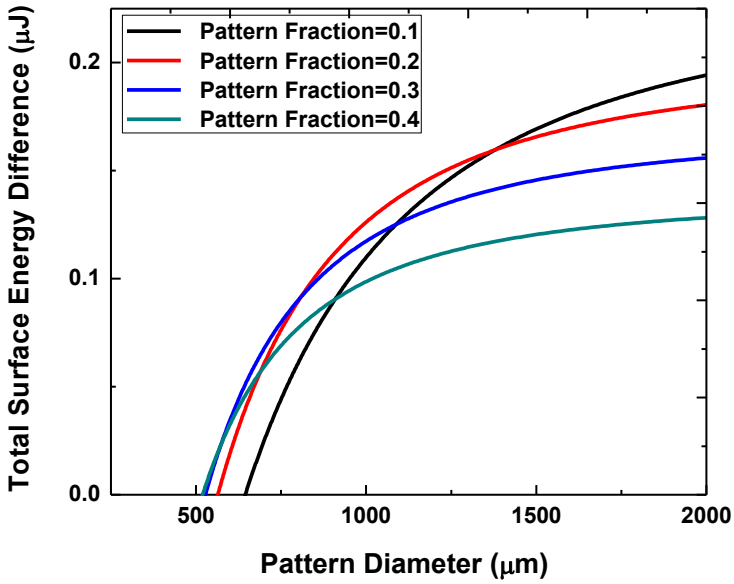

(a)

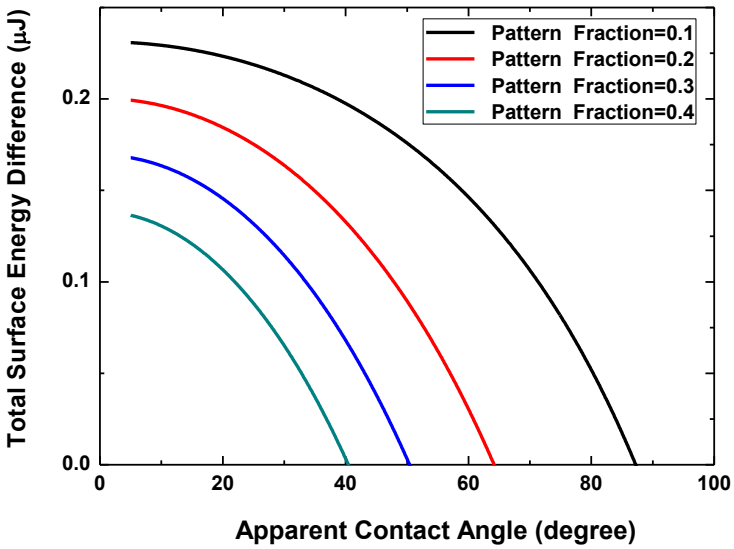

(b)

Figure 2.4: Interface energy difference with different pattern sizes and densities (a), or with different apparent angles of the discrete droplets (b).

2.2.2 Rupture Distance and Capillary Forces

We use the surface energy minimization algorithm to predict the equilibrium configuration of a liquid bridge as a function of spacing between the two bounding solid surfaces. The configuration (or shape) of the liquid bridge that minimizes the total interfacial energy is found using an iterative algorithm implemented using Surface Evolver [31-32]. The maximum gap below which the liquid bridge remains the most stable configuration is set as the rupture distance.

The rupture distance is also experimentally measured using a dual camera setup to observe the side and top view of a liquid bridge formed between a transparent glass top substrate and a silicon substrate. The side view images are used to quantify the droplet or bridge profiles and check the parallelism of the two substrates. The top view is used to determine the liquid film thickness from the known liquid volume and the observed area of the liquid layer. The top substrate is mounted on a precision z-stage to control the gap between the substrates. The resolution of the imaging system is approximately 5 μm. Figure 2.5 shows representative optical images obtained while raising the top substrate.

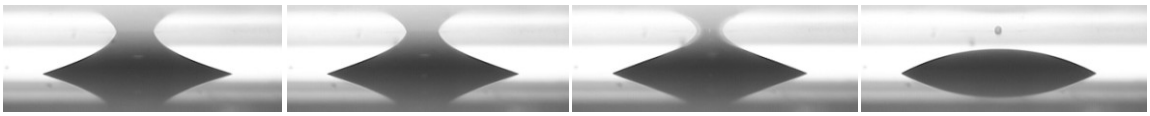

Figure 2.5: Cross sectional images illustrating morphological transition at the rupture point.

Figure 2.6 shows the predicted and measured rupture distances for samples with three different hydrophilic pattern sizes (0.5 mm, 1 mm and 1.5 mm) and for five different values of the pattern areal fraction, f. The total volume is fixed at 0.7 μL with the target minimum gap g of 20 μm. The rupture distance decreases with increasing f because the height of discrete liquid droplets on each hydrophilic pattern is smaller at higher pattern areal fractions, for a given total liquid volume. For a given areal fraction, the rupture distance also scales roughly with the pattern size. The prediction agrees well with the measured rupture distances for all the cases examined here.

When the design goal is to achieve a small rupture distance, one would prefer smaller pattern sizes and higher areal fractions. This requirement, however, conflicts with the requirement for achieving the reversibility discussed in the preceding section. One may therefore select the smallest acceptable pattern size for reversible switching to minimize the rupture distance.

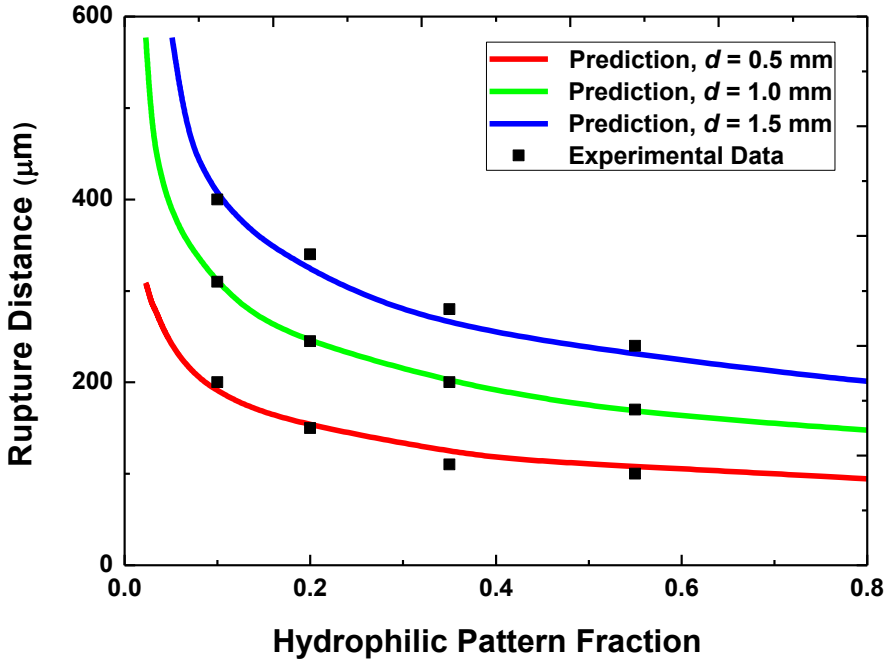

Figure 2.6: Rupture distances with different pattern sizes and areal fractions.

Another important mechanical characteristic of liquid-based interfaces is the force-gap relation. We predict this relation using the virtual work model in conjunction with the surface energy minimization algorithm. The capillary force is computed as the first derivative of the interfacial energy of the equilibrium configuration: $F = -dE/dg$. The force-gap relation is also experimentally characterized by placing a bottom substrate on a precision balance to measure the force and reducing (or increasing) the gap between the two substrates using the precision z-stage.

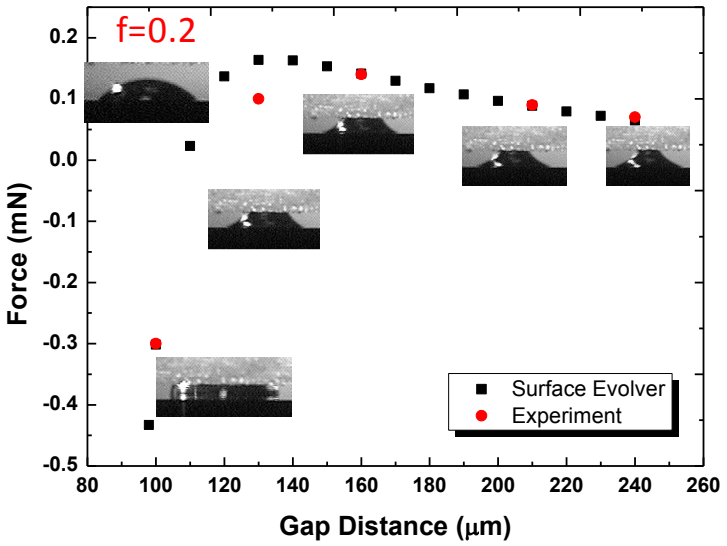

(a)

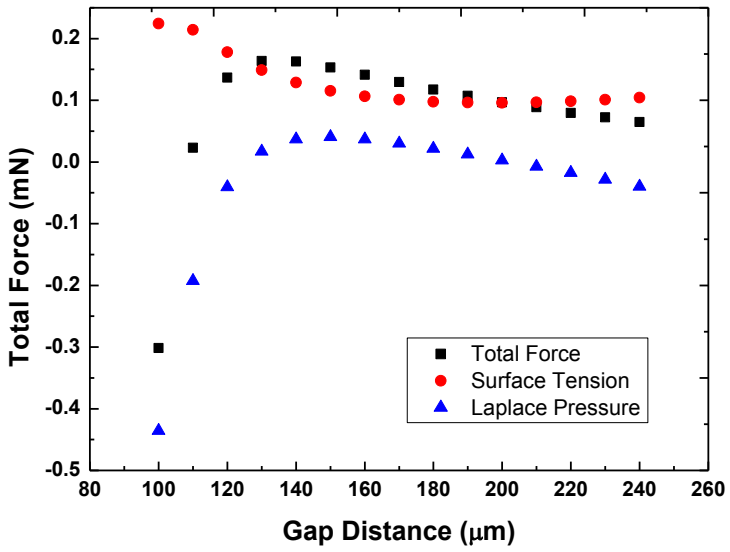

(b)

Figure 2.7: (a) The total capillary force as a function of gap distance for interfaces with areal fraction of 0.2, also shown is the liquid morphology. (b) Contributions from the Laplace pressure and the surface tension.

Figure 2.7(a) shows the total capillary force the substrates experience at different locations. Side-view images of the droplet shapes are captured to get the exact gap distance, the wetting areas and contact angles of both substrates. The contributions from the Laplace pressure and the surface tension are analyzed using Surface Evolver, as shown in Figure 2.7(b). As the gap distance is increased, the attractive component of the surface tension force exceeds the repulsive component, and the net force becomes positive. The contact angle as well as the wetting area and perimeter of the top substrate will change along with the gap distance (Figure 2.8). The repulsion Laplace pressure decreases due to the rapid change of bottom apparent contact angle and then surface tension becomes dominant. The attractive pressure may decrease for some pattern fraction because of the shrink of wetting diameter at the top substrate.

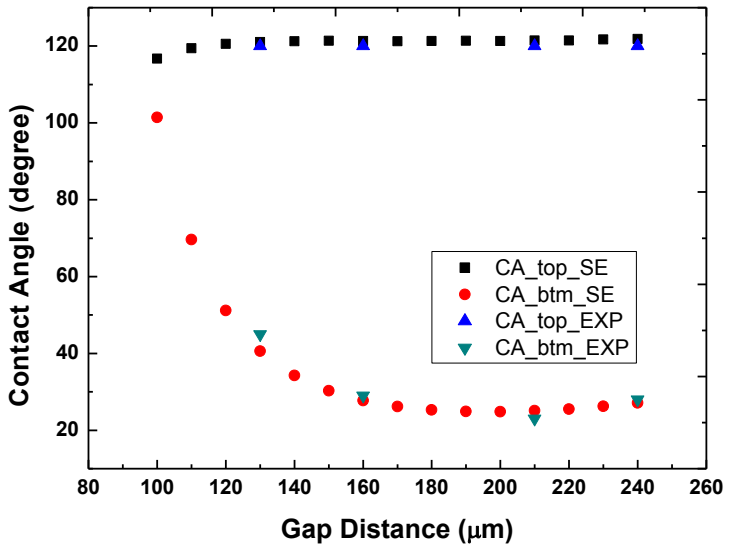

(a)

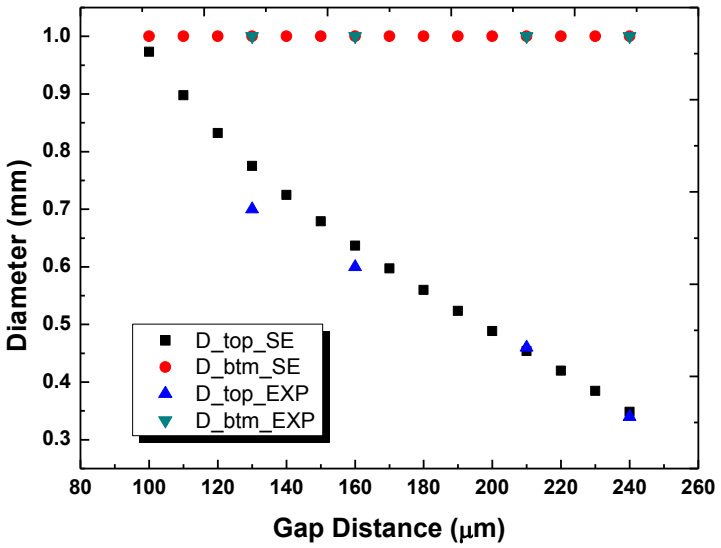

(b)

Figure 2.8: The (a) contact angles and (b) wetting diameters of the droplet on both substrates at different gap distances.

Figure 2.9 shows the measured and predicted loading pressure as a function of gap for substrates with the fixed pattern diameter of 1 mm. In transitioning from the off- to on-state, multiple liquid bridges are first formed between the two substrates. In the multiple-bridge state, the different curves in the figure correspond to different values of the pattern areal fraction, *f*. These curves then merge into one universal curve once a continuous thin film is formed. The effect of contact angle hysteresis is small.

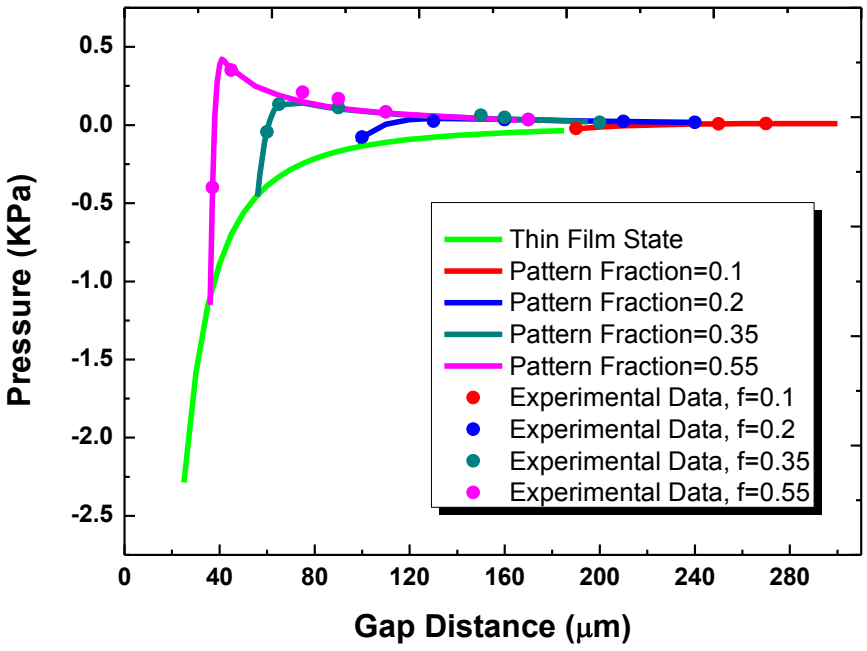

Figure 2.9: The pressure as a function of gap distance at thin film state and multi-bridge state.

The total work required for one switching operation (on and off) may be calculated as the sum of the work necessary to push the substrates to achieve a desired gap distance (work of actuation) and the work necessary to pull the substrates and cause rupture (work of separation). Table 2.1 shows the values obtained by integrating the loading force as a function of gap distance for substrates with the fixed pattern diameter of 1 mm. They are compared with the difference between the total surface energies between the discrete multi-droplet state and the thin-film state.

Pattern Fraction	Energy Difference (μJ)	Total Work (μJ)	Work of Actuation (μJ)	Work of Separation (μJ)
0.1	2.1	2.2	2.2	0.02
0.2	1.8	1.9	2.0	0.13
0.35	1.2	1.4	1.7	0.28
0.55	0.5	0.88	1.3	0.47

Table 2.1. The total operation work with different pattern areal fractions.

2.2 Thermal Resistance Characterization and Life Testing

Figure 2.8 schematically shows the experimental setup we use for thermal resistance measurements. We use a serpentine metal strip microfabricated on a glass slide (top substrate) as a heater and electrical resistance thermometer to characterize the thermal resistance of liquid layers (on-state interface thermal resistance). We apply a current pulse to the heater and monitor resulting changes in its electrical resistance and hence temperature as a function of time. The temporal temperature profile is then analyzed using finite element simulations to extract the thermal resistance.

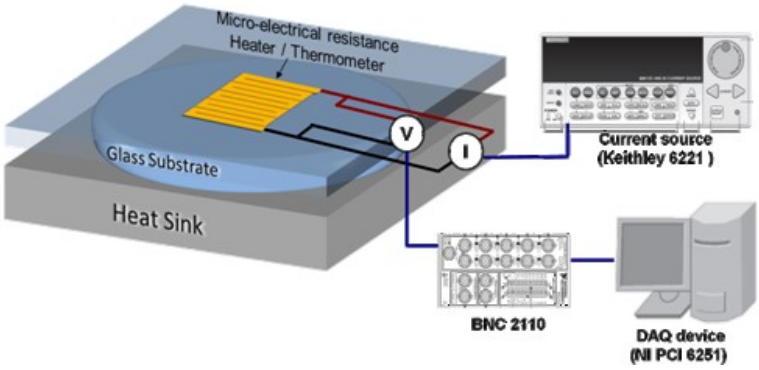

Figure 2.10: Schematic of the measurement setup for thermal resistance (transient hot disk technique).

We use de-ionized water for the experiments discussed in the preceding sections for the capillary force and rupture distance because it allows the surfaces to be readily cleaned and reused. For practical applications, non-volatile liquids, such as hydrophobic ionic liquids (e.g., [BMIM][BF_4] and [DMPI]Im) [33], may be more suited. We picked two commercial available ionic liquids [BMIM][BF_4] and [BMIM][PF_6] for further test. Please check if they are right.

Figure 2.9 shows the experimentally measured temporal temperature profiles and the corresponding FEM simulation results. The thickness of the [BMIM][BF_4] layer is 12 μm and the thickness of the [BMIM][PF_6] layer is 10 μm. The initial parts of the temporal profiles (not shown) are governed primarily by heat conduction through the glass slide and not sensitive to the thermal resistance of the interface.

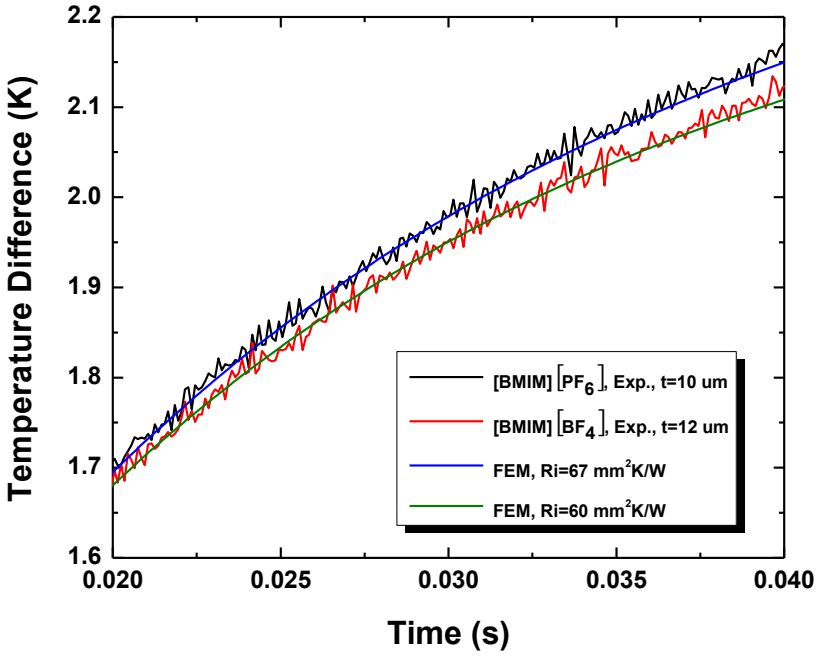

Figure 2.11: Temporal temperature profiles obtained during experiments and the best fits obtained using finite element simulations.

From the measured thermal resistance and liquid layer thickness, we determine the thermal conductivity of [BMIM][BF_4] to be 0.19 ± 0.01 W/mK and that of [BMIM][PF_6] to be 0.15 ± 0.01 W/mK. These compare well with the literature values of bulk samples, 0.186 W/mK and 0.145 W/mK, respectively. This suggests that the thermal boundary resistance at liquid-solid interfaces, which arise from finite mismatch in the acoustic (phonon) properties of the two substances, is negligible compared with the bulk thermal resistance of the liquid layers.

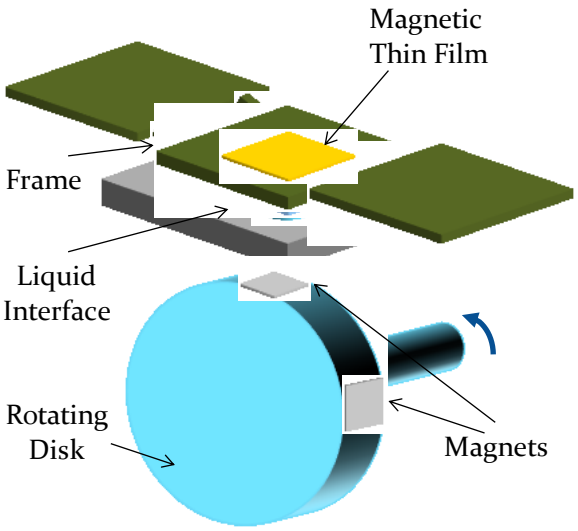

(a)

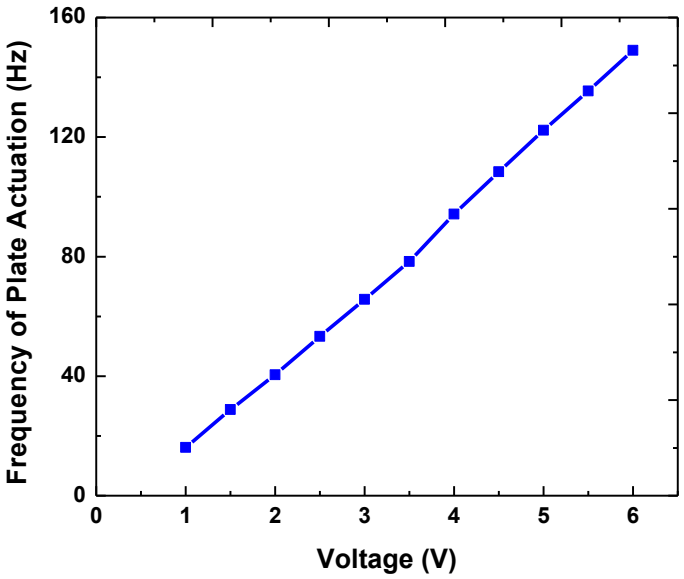

(b)

Figure 2.12: (a) Schematic of the life testing setup; (b) Plate actuation frequency as a function of voltage applied to the DC motor.

To obtain preliminary evaluation of the reliability of the present switchable interfaces, we constructed an experimental setup shown in Figure 2.10. A spring-supported frame bonded with a magnetic foil is actuated by rotating a disk embedded with multiple permanent magnets. The frame is separated from the disk by a substrate containing a switchable liquid-based interface. The disk was rotated using a DC motor to actuate the plate up and down and make mechanical contacts with the interface at a controlled frequency. The liquid interfaces were shown to operate reliably at frequencies as high as 20 Hz for at least 1,000 h. For some ionic liquids, such as [BMIM][PF_6] that contain fluorine atoms [34], the total liquid volume decreases with time due to formation of volatile species through hydrolysis. This may lead to interface failure when the liquid droplets are depinned from the pattern boundaries. Such problems were not observed in other ionic liquids, including 1-ethyl-3-methylimidazolium dicyanamide.

2.3 Summary

The present work establishes a concept for switchable thermal interfaces based on an array of discrete liquid droplets initially confined on hydrophilic islands on a substrate. The droplets undergo reversible morphological transition into a continuous liquid film when they are mechanically compressed by an opposing substrate to create low-thermal resistance heat conduction path. We investigate a criterion for reversible switching in terms of hydrophilic pattern size and liquid volume. The dependence of the liquid morphology and rupture distance on the diameter and areal fraction of hydrophilic islands,

liquid volumes, as well as loading pressure is also characterized both theoretically and experimentally. The thermal resistance in the on-state is experimentally characterized for ionic liquids, which are promising for practical applications due to their negligible vapor pressure. A life testing setup is constructed to evaluate the reliability of the interface under continued switching conditions at relatively high switching frequencies.

CHAPTER 3

Solid-Liquid Hybrid Thermal Interfaces for Low-Contact Pressure Thermal Switching

In this chapter, we discuss a solid-liquid hybrid thermal interface for reliable low-contact pressure (< 1 kPa) switching with on-state thermal contact resistance < 15 $x10^{-6}$ m^2K/W. Reduction in the thermal resistance of hybrid interfaces created through electroplating was evaluated using transient pulsed heating measurements and thermal time constant characterization. Compared with pure liquid-mediated interfaces and direct solid-solid contacts reported previously, the hybrid interface shows superior thermal performance under the same loading pressure while avoiding the use of liquid metals. The hybrid interface may be readily used with low-power electrostatic or Lorenz force-based actuators as part of integrated thermal micro-devices.

3.1 Background

Our recent studies [14, 35] demonstrated liquid-based switchable thermal interfaces that can circumvent drawbacks of conventional and nano-engineered direct solid-solid contacts, including requirements of very large loading pressure and various failure mechanisms such as fracture, cold welding, incomplete contact due to debris, and delamination of interfacial layers [11, 13].

Further reduction in the actuation (switch-on) loading pressure, however, is needed before one may incorporate these interfaces into MEMS devices. Electrostatic or electromagnetic forces very often used in micro-devices are relatively weak at length scales of the order of 100 μm, which is necessary for reliable switching and high on/off ratios.

We now report an improved switchable thermal interface where an array of micromachined metal posts is embedded in a capillary confined liquid droplet to significantly enhance heat conduction in the on-state. Figure 3.1 schematically illustrates the solid-liquid hybrid interface design concept. This hybrid interface design allows us to achieve a low thermal resistance at much reduced loading pressure while avoiding the use of liquid metals, which either pose health and environmental hazard or oxidize rapidly in the ambient air.

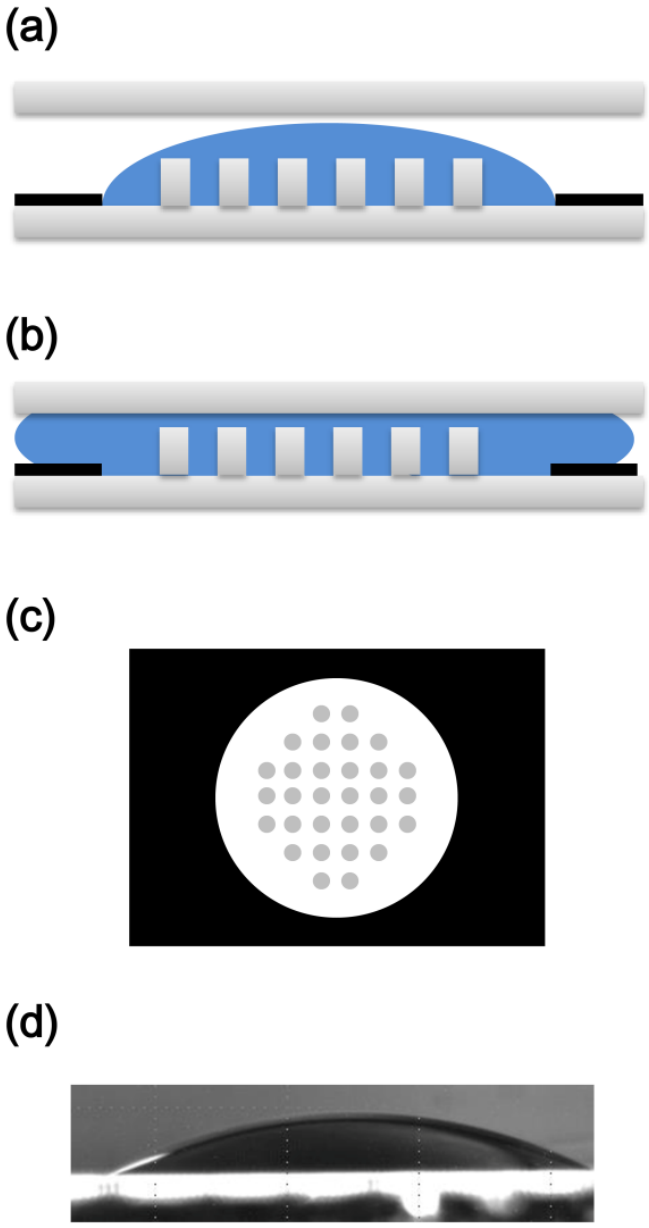

Figure 3.1: Solid-liquid hybrid interface: (a) off-state; (b) on-state; (c) top view of the mask pattern; (d) side view of the droplet after being deposited in the circular hydrophilic region incorporating microposts.

3.2 Sample Preparation

The hybrid interface was prepared by electroplating Cu through a lithographically defined photoresist mold and forming an array of Cu microposts, as shown in Figure 3.2. Briefly, we first deposited a seed layer (30 nm Ti / 350 nm Cu / 30 nm Ti) on a silicon substrate using e-beam thermal evaporation (CHA Mark 40). We note that, although we used silicon substrates pre-coated with such a seed layer in the present work, the versatile electroplating approach can be readily adapted to any electrically conducting substrates to create the liquid-solid hybrid interfaces. We spin coated a negative photoresist (PR) layers on the substrate and lithographically patterned it to create an array of through-holes as a mold. We next removed the protective Ti layer and the native oxide layer formed on the seed layer under the through-holes using a diluted solution of hydrofluoric acid. The sample was then immersed in a commercial Cu electroplating bath and a low initial plating current density (~ 1 mA/cm^2) was applied to facilitate the formation of good electrical and mechanical contacts between the electrochemically deposited copper and the seed layer. Once electrodeposition was activated in all through-holes, the current density was increased (~ 7 mA/cm^2) to achieve higher deposition rates. After the completion of the electrodeposition, the sample was rinsed multiple times and the PR layer was stripped to expose the Cu micropost array.

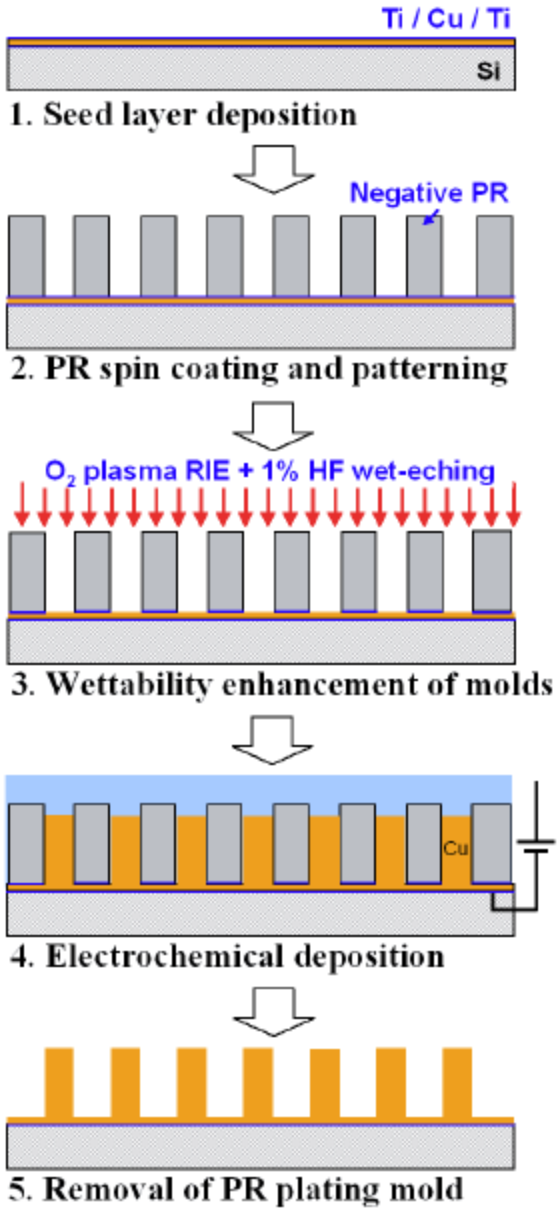

Figure 3.2: Fabrication process flow of Cu microposts. [36]

Figure 3.3 shows the SEM image of microposts of diameter 100 μm, height 65 μm, and solid fraction (areal fraction of the microposts) 20% after the photoresist layer was removed. The microposts were confined within a circular region of diameter 6 mm (Fig.

3.1c). A hydrophobic Teflon layer was applied outside the region through contact printing. A droplet of water was next deposited on the hydrophilic region (Fig. 3.1d) to form a liquid-solid hybrid interface.

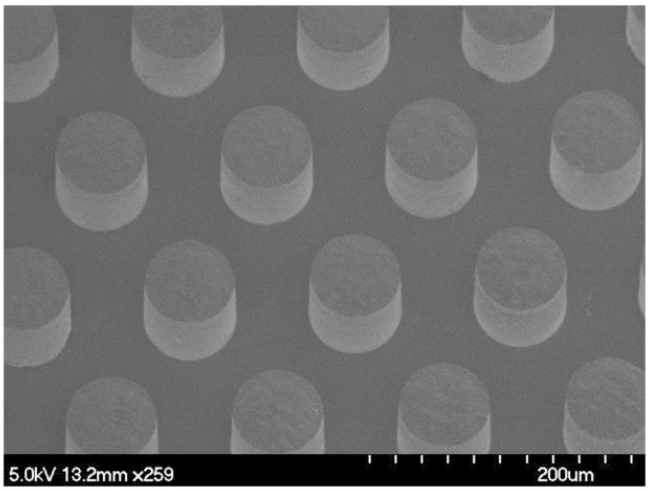

Figure 3.3: SEM of Cu microposts fabricated using the electrodeposition technique.

3.3 Mechanical Characteristics

One important characteristic of the switchable thermal interfaces is the force-gap relation, in particular, the maximum loading force required to balance the capillary forces and achieve the on-state where two surfaces defining the interface are pressed against each other until the liquid layer thickness and hence the interface thermal resistance reaches the targeted minimum value. In previous studies, we and others predicted such relations for liquid bridges using the virtual work model in conjunction with the surface energy minimization algorithm and validated them experimentally [14].

For the present liquid-based switchable interfaces, the in-plane liquid droplet diameter (> 6 mm) is much larger than the gap (~ 100 μm). The liquid meniscus can therefore be reasonably modeled using an arc approximation. One can then write an approximate analytic expression for the capillary force, which is the sum of the contributions from the Laplace pressure and the surface tension, as

$$F_s \approx 2\sigma\pi\sqrt{\frac{V}{\pi d}}\sin(\theta) + \sigma\left(\frac{2\cos(\theta)}{d^2}V - \sqrt{\frac{\pi V}{d}}\right)$$

Here, σ is the surface tension coefficient of the liquid-air interface, d is the gap between the substrates, θ is the apparent contact angle, and V is the liquid volume. For small gaps, the second term representing the Laplace pressure dominates over the first term representing the surface tension force. For a pinned liquid bridge, where the liquid contact area remains constant, the liquid volume V varies approximately in proportion to the gap d. As a result, the capillary force scales approximately as $F_s \sim V/d^2 \sim 1/d$.

For an interface thickness (or gap) of 75 μm, the corresponding loading pressure is only about 1 kPa for water despite its relatively high surface tension. We use de-ionized water in the present study because it allows the surfaces to be readily cleaned and reused. For practical applications, non-volatile liquids, such as ionic liquids with nearly zero vapor pressure, may be more suited to minimize or possibly eliminate a need for refilling the interfaces.

3.4 Thermal Charateristics

3.4.1 Thermal Resistance Characterization

To experimentally characterize the thermal resistance of our thermal interfaces, we used a thin-film serpentine heater lithographically patterned on one side of a silicon substrate. The other side of the substrate was coated with a layer Teflon to render it hydrophobic.

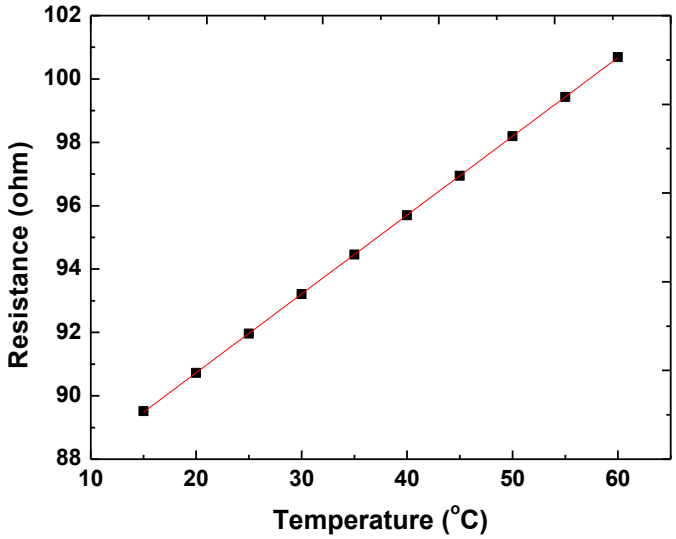

Figure 3.4: Temperature coefficient of resistance of the thin-film heater obtained from independent experiments.

We used the same experimental setup in the previous chapter for the characterization of the thermal resistance of our interfaces. Figure 3.4 shows the temperature coefficient

of resistance of the thin-film heater. We applied a current pulse of a precisely defined amplitude to the serpentine heater and obtained temporal changes in its temperature by monitoring the temperature-dependent electrical resistance using a data acquisition system equipped with a 16-bit analog-to-digital converter. Each temporal temperature profile (Figure 3.5) was then analyzed using 3D transient finite element simulation to extract the thermal resistance across the interface.

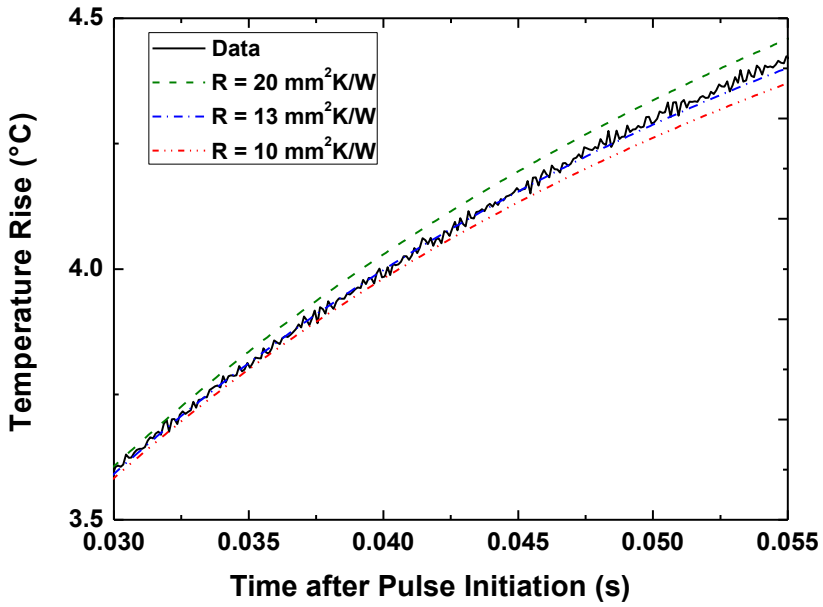

Figure 3.5: Example temperature profiles obtained from measurements and FEM simulations.

Figure 3.6 shows the thermal resistance of the hybrid interface as a function of the interface thickness. The inverse of the slope of a linear fit to the thermal resistance versus

thickness data is approximately 0.6 W/m K, which agrees with the thermal conductivity of liquid water. This result is consistent with the fact that the effective thermal resistance of the Cu micropost array (0.9×10^{-6} m^2K/W), calculated using the thermal conductivity of an electroplated Cu film, is negligible. The total thermal interface resistance is therefore dominated by that of the thin liquid overlayers sandwiched between the top plane of the microposts and the top substrate. The thermal conductivity of the Cu film (350 W/m K) was obtained from the measured electrical resistivity using the Wiedemann-Franz law. At the same micropost height of 65 μm, micropost arrays of lower solid fractions, down to approximately 10%, may still provide sufficiently small thermal resistance (< 10 percent of the liquid overlayer resistance).

The measured thermal resistance of the present 75 μm-thick hybrid interface is 13×10^{-6} m^2K/W, which is equivalent to that of a 10 μm-thick pure (without microposts) liquid water layer. Since the capillary force is approximately inversely proportional to the interface thickness, we therefore can achieve as much as 7 fold reduction in the loading pressure necessary to achieve the same thermal resistance for this particular sample.

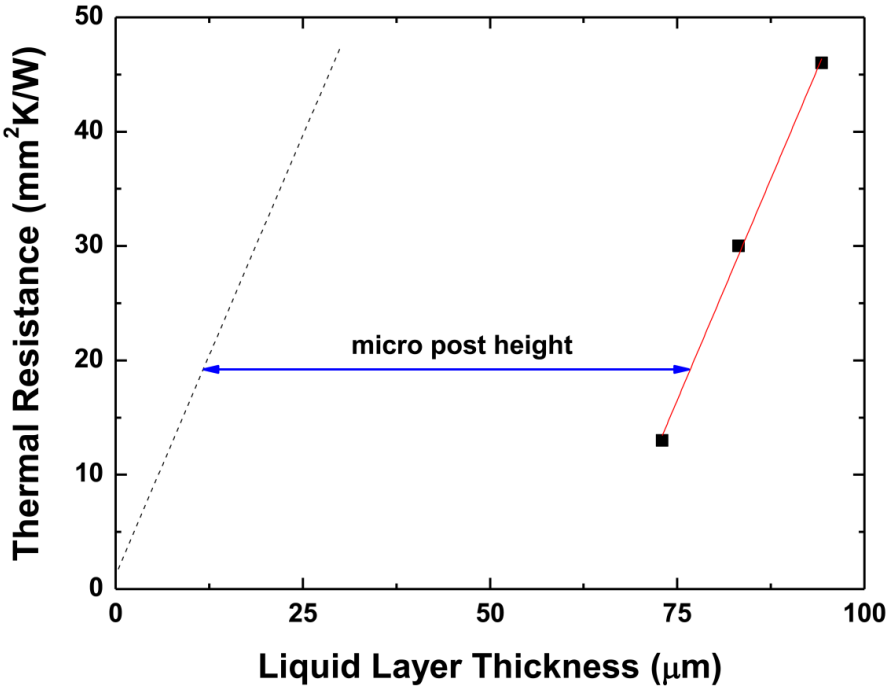

Figure 3.6: Experimentally determined thermal resistance of the hybrid interface as a function of the liquid layer and hence the interface thickness.

3.4.2 Thermal Time Constant Measurement

To further demonstrate the thermal performance benefit, we measured the thermal time constant of a thin plate that was made into a sudden contact with a hot reservoir through three different thermal interfaces: a direct solid-solid contact, a liquid thermal interface, and a liquid-solid hybrid thermal interface. The thin plate emulates a ferromagnetic actuation plate in previously reported thermomagnetic energy harvesters and thermal switches [37] and a thin-film pyroelectric or electrocaloric material for previously reported thermal-to-electric energy conversion and refrigeration devices [7,8].

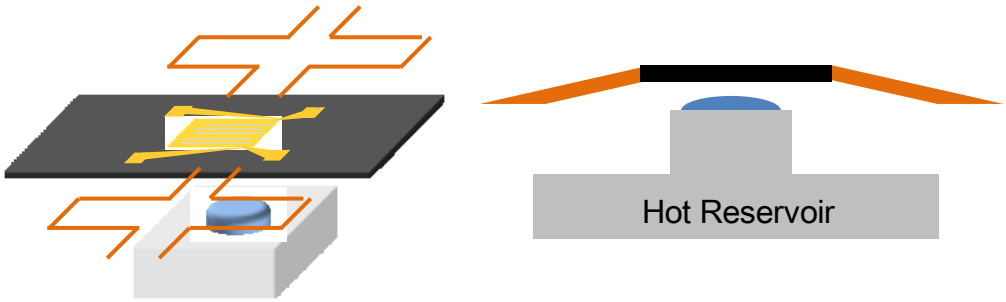

(a) **(b)**

Figure 3.7: Experimental setup for thermal time constant measurements.

As shown in Figure 3.7, an aluminum block with an embedded thermistor was used as a hot thermal reservoir. Its temperature was controlled by adjusting power input to a Peltier device attached on the bottom. Three silicon substrates, each incorporating one of the three different thermal interfaces, were mounted on the aluminum block using thermal grease. We used a thin silicon actuation plate with a built-in thin-film resistance thermometer to monitor its temperature as a function of time after contact with the hot thermal reservoir. The plate was attached to a spring frame using epoxy dots of low thermal conductivity. The spring constant of the frame was pre-calibrated by hanging a set of reference weights and monitoring the resulting deflections. The spring frame itself was mounted on a motorized translation stage so that we could control and monitor the gap spacing/spring deflection using a high-speed digital camera.

For each experiment reported here, we maintained loading pressure to a target value of approximately 0.5 kPa (± 0.1 kPa) to ensure fair comparison among the three thermal interfaces. This loading pressure is of the order of the electrostatic pressure expected at a bias voltage of 100 V across a 100 μm-thick water layer.

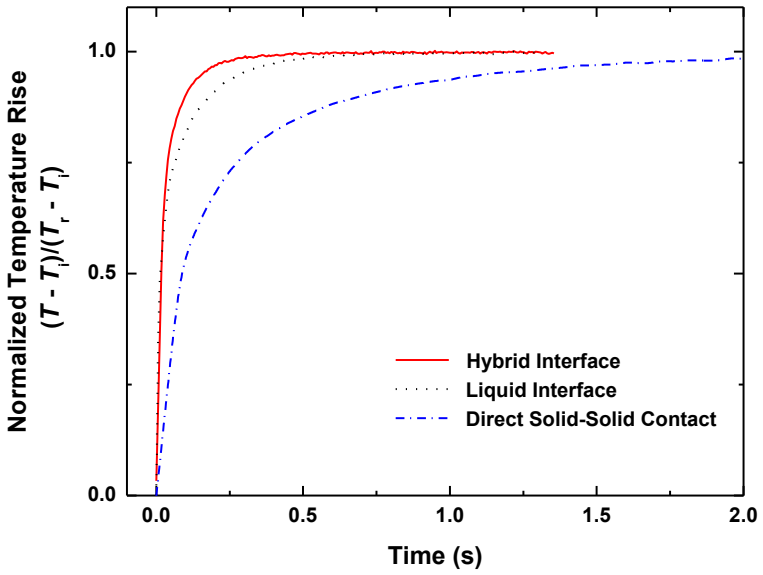

Figure 3.8: Normalized temporal temperature profiles of the actuation plate in contact with the hot reservoir through the three different interfaces.

Figure 3.8 shows the normalized temperature rise in the actuation plate as a function of time after contact for the three different thermal interfaces. As expected, the direct solid-solid contact requires the longest time for the plate to reach the reservoir temperature and hence has the largest thermal resistance. The solid-liquid hybrid

interface outperforms the pure liquid interface even though the total interface thickness and hence the loading force remain the same.

Under the lumped capacitance model, the thermal time constant τ can be related to the thermal interface resistance:

$$\frac{T - T_i}{T_r - T_i} = 1 - \exp\left(-\frac{t}{RC}\right) = 1 - \exp\left(-\frac{t}{\tau}\right)$$

Here, T is the temperature of the actuation plate, T_r is the temperature of the hot reservoir, T_i is the initial temperature of the actuation plate, t is the time after contact with the hot reservoir, C is the thermal capacitance of the actuation plate, and R is the thermal interface resistance.

The thermal time constants extracted by analyzing the data using the lumped capacitance model are 350 ms, 135 ms, and 75 ms for the direct solid-solid contact, the liquid interface, and the hybrid interface, respectively. The latter two values compare reasonably well with the thermal time constants (150 ms and 70 ms) calculated using the independently measured thermal interface resistance values. Even for the relatively large gap used here, the hybrid interface offers almost 5-fold reduction compared with the direct solid-solid contact and almost 2-fold reduction compared with the pure liquid interface.

3.5 Summary

In summary, we successfully demonstrated a solid-liquid hybrid thermal interface for reliable low-contact pressure (< 1 kPa) switching with on-state thermal contact resistance < 15 x10^{-6} m^2K/W. Compared with the liquid-mediated interface and the direct solid-solid contact, it shows superior thermal performance under the same loading pressure. Such interfaces may be readily used with low-power electrostatic or Lorenz force-based actuators as part of integrated thermal MEMS devices.

CHAPTER 4

Solid-State Refrigerator Based on the Electrocaloric Effect and the Liquid-Based Switchable Thermal Interface

In this chapter, we demonstrate a new device concept of a compact solid-state cooling module based on the giant electrocaloric effect. Our novel design realizes controllable thermodynamic cycles for the ferroelectric material thin films with laterally interdigitated electrodes. It also exploits the liquid-based thermal interfaces to enable reliable and high-contrast thermal switching and at the same time offer high off-state resistance to minimize deleterious parasitic heat transfer. We numerically simulate the cooling performance, as well as experimentally confirm ~1 K temperature drop at the operation frequency of ~0.3 Hz.

4.1 Background

As discussed in the Chapter 1, the EC refrigerators offer an intriguing alternative to the Peltier coolers, but face a number of technical challenges in implementation, such as high parasitic loss and slow heat diffusion in EC materials. Figure 4.1 schematically shows our innovative EC cooling module. The laterally interdigitated electrode assembly, which is infiltrated with the EC material, is actuated up and down to make alternating thermal contacts with the cooling load or heat sink. By applying and removing electric fields in concert with the mechanical motions, we subject the EC material to controlled thermodynamic cycles.

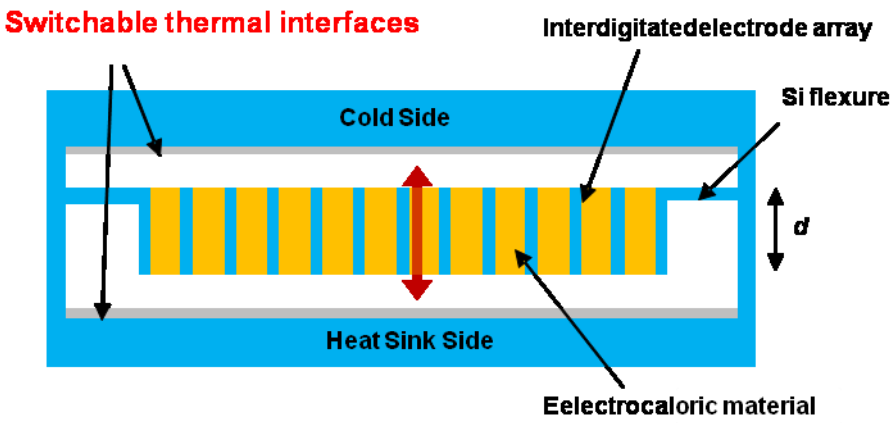

Figure 4.1: Schematic cross-sectional diagram of a single-stage EC cooling module.

The cooling module densely stacks multiple EC films laterally as opposed to vertically so that the electrodes with high thermal conductivity enable rapid heat diffusion.

Meanwhile, switchable liquid-based thermal interfaces discussed in the previous chapters enable reliable and fast thermal switching while virtually eliminating various reliability challenges of direct solid-solid contacts (e.g., cold welding, fracture, debris). A key feature of our thermal switching scheme is that it provides high off-state thermal resistance ($R_{off} > 10^{-2}$ m^2K/W) as well as high switching ratio ($R_{off}/R_{on} > 100$). [14, 35, 38] Thus our cooling module is ready to overcome the limitations of existing designs.

4.2 Experiment Details

As in vapor compression cycles, different thermodynamic cycles can be used to exploit the EC effect for refrigeration [16]. An ideal Carnot cycle was described in previous studies [18]. Alternative cycles developed for pyroelectric energy conversion [39-40] may also be adapted for EC cooling. Figure 4.2 schematically illustrates another possible cycle on a T-S diagram, which is more straightforward to implement. The cycle consists of the following: (1) polarization step: from state A to state B, the EC material experiences electrocaloric heating as the electric field is raised adiabatically; (2) heat rejection step: the material subsequently rejects heat under the constant electric field to reach state C; (3) depolarization step: from state C to state D, the material experiences electrocaloric cooling as the electric field is reduced adiabatically to its minimum value; (4) heat absorption step: the "cold" EC material is then brought into thermal contact with an electronic device to absorb heat under the constant electric field and returns to state A.

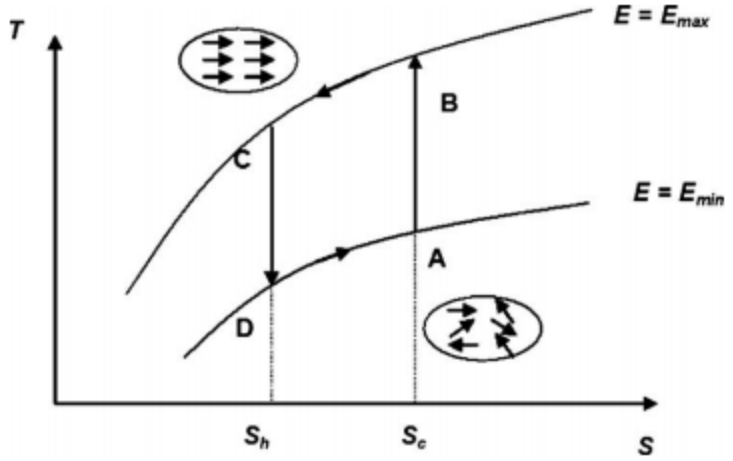

Figure 4.2: T-S diagram of one potential thermodynamic cycle for EC refrigeration.

Figure 4.3 schematically shows our experimental setup to implement and characterize the EC Brayton cycle. We use doped $BaTiO_3$ ferroelectric layers in a multilayer capacitor discussed in recent articles as the electrocaloric material. The capacitor is mechanically actuated up and down using amotorized z-stage to make alternating thermal contacts with a heat source (cooling load) or a heat sink. By synchronizing the application and removal of bias electric fields with the mechanical motions, we subject the EC material to a controlled thermodynamic cycle. The interdigitated electrode layers are oriented parallel to the direction of heat transfer to facilitate heat diffusion.

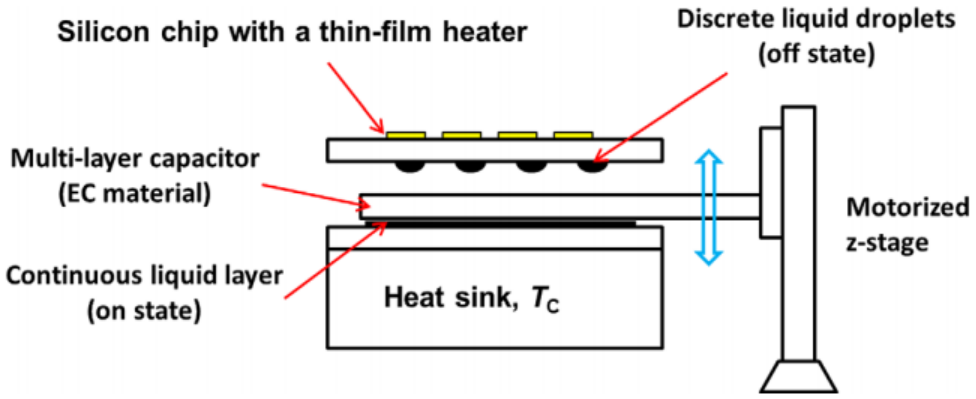

Figure 4.3: Experimental setup used to characterize the electrocaloric cooling cycle.

We use a thin-film serpentine Au heater fabricated on a 100 μm-thick silicon substrate as a heat source (cooling load). The small thermal mass of this heat source facilitates tracking of transient thermal energy transport through monitoring of temporal variations in the heater temperature.

To form liquid-based switchable thermal interfaces, the backside of the heater chip and the top surface of the heat sink were first coated with layers of Teflon®. The Teflon® layers were then lithographically patterned to form circular hydrophilic islands of diameter approximately 1 mm. Liquid droplets dispensed onto these islands undergo reversible morphological transformation between the discrete droplet state (thermal contact off) and the continuous thin-film state (thermal contact on). The hydrophilic islands allow us to form droplets only on pre-defined locations and to control their volumes and hence detachment distance, taking advantage of the predominance of surface tension in sufficiently small droplets.

We select glycerol as an interface liquid in the present study due to its relatively high contact angle (approximately 110°) on Teflon® and a low vapor pressure. Ionic liquids with virtually zero vapor pressure may be used in practical refrigerators to minimize liquid loss from evaporation.

4.3 Results and Discussion

4.3.1 Direct Characterization of the EC Effect

We first characterize the EC properties of a stand-alone multi-layer capacitor. A triangular voltage waveform with a peak amplitude of 400 kV/cm and a frequency of 15Hz is applied to the capacitor, and the electric displacement D is measured using the Sawyer-Tower circuit to construct the D-E hysteresis curve (Figure 4.4). The data show a small hysteresis loss of <5%, attractive for practical refrigerator applications.

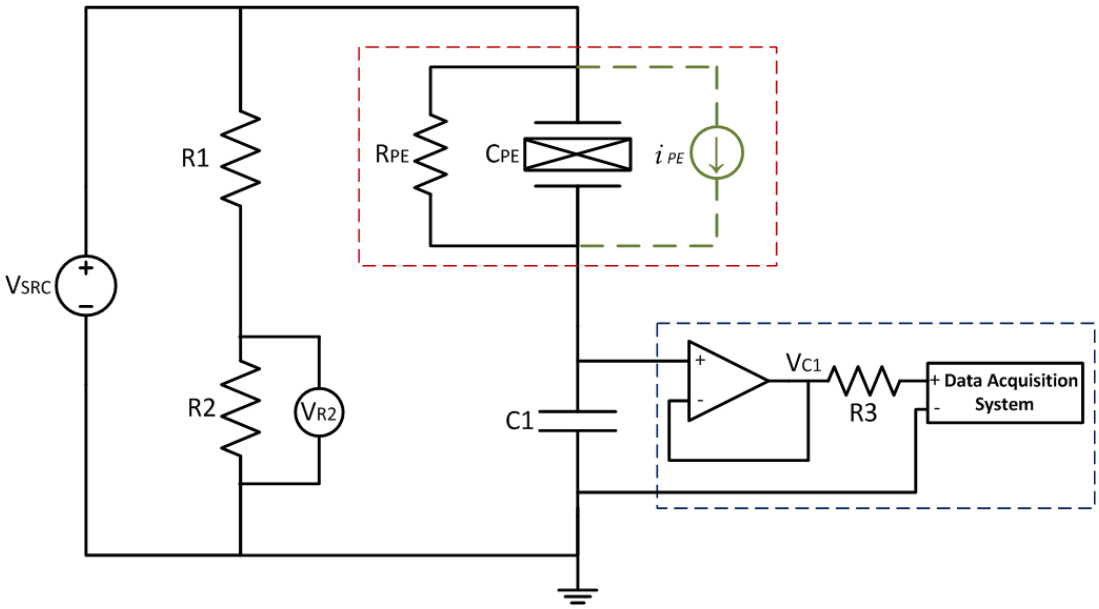

(a)

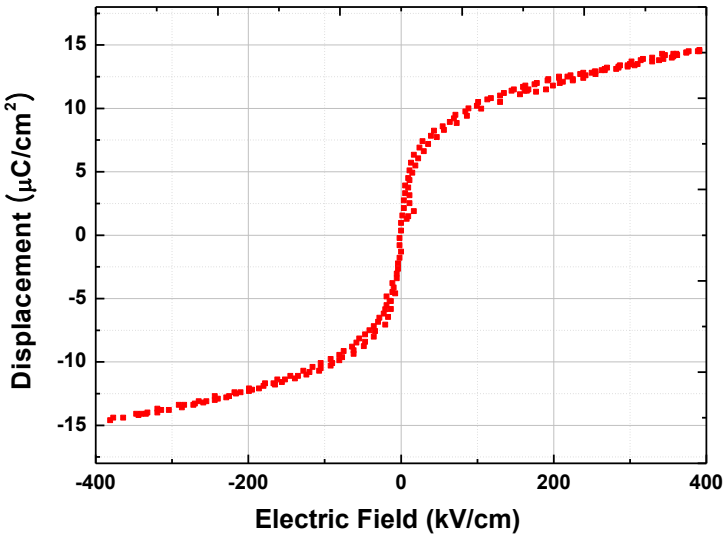

(b)

Figure 4.4: (a) Sawyer-Tower circuit with a voltage follower. (b) Hysteresis loop at room temperature.

A small-diameter (~50 μm) K-type thermocouple bead is next attached to the capacitor to estimate the adiabatic temperature change for later use in our thermal model. The measurement results are shown in Figure 4.5. The red line indicates the ambient temperature. Upon application of a bias field of 300 kV/cm, the temperature increases sharply by ~0.5K due to electrocaloric heating. The thermal energy then slowly leaks through a parasitic thermal link to the ambient, causing the temperature to return to the ambient temperature. A subsequent removal of the electric field produces a sudden decrease in temperature due to electrocaloric cooling. Small hysteresis losses and Joule heating make the magnitude of the temperature drop due to electrocaloric cooling slightly smaller than that of the temperature jump due to electrocaloric heating. Our measured electrocaloric temperature changes agree well with the results from a previous study on a nominally identical capacitor.

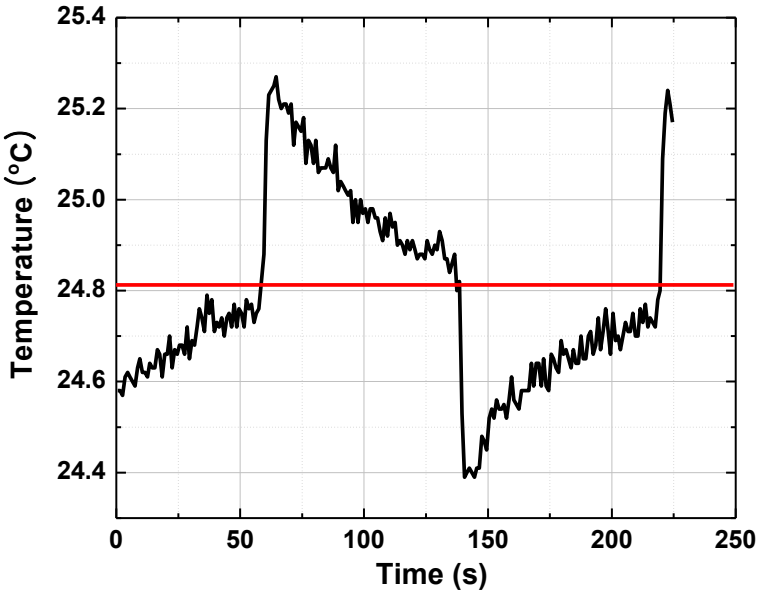

Figure 4.5: Temporal temperature profile upon application and removal of a bias field of magnitude 300 kV/cm.

4.3.2 Device Level Cooling Performance

The EC refrigeration cycle is next implemented using a multi-layer capacitor. A constant current was applied to the heater to induce Joule heating at approximately 15mW and set its unperturbed steady state temperature of approximately 27 ℃. This heating power corresponds to a power density per area of 2.5 kW/m^2. The heat sink was maintained at the ambient temperature 25.7 ℃. The heater temperature was measured by using the thin film heater as an electrical resistance thermometer and also using a small-diameter (~50 μm) K-type thermocouple bead attached to the heater.

Figure 4.6 shows the measured transient temperature readings of the heater under different operating conditions. To set a baseline, we first mechanically actuate the EC capacitor without applying any bias electric field, that is, without inducing any electrocaloric cooling. Under this mechanical-motion-only (MMO) condition, the EC material and electrode assembly passively shuttles the thermal energy generated by Joule heating in the heater to the heat sink. As a result, the heater temperature undergoes oscillations, reaching a steady periodic condition at the same frequency as the mechanical motions. The cycle period is a sum of the residence times on both the heater surface and the heat sink surface (~ 3.5 s in the specific case shown in Figure 4.6) and a finite round-trip mechanical traveling time between the two surfaces (~ 1 s).

We next apply bias voltages in concert with the mechanical motions to implement the EC refrigeration cycle. Under this EC condition, the temperature of the EC material-electrode assembly is reduced below that of the heat sink (Process Step 3 in the Brayton cycle) through EC cooling right before the assembly makes a thermal contact with the heater. The increased temperature difference between the heater and the assembly leads to corresponding increase in heat transfer rate. The heater temperature is thereby decreased below that under the MMO condition. Once the assembly is thermally detached from the heater, the temperature of the latter increases back due to continued Joule heating. The heater reaches a second steady periodic state after a few cycles.

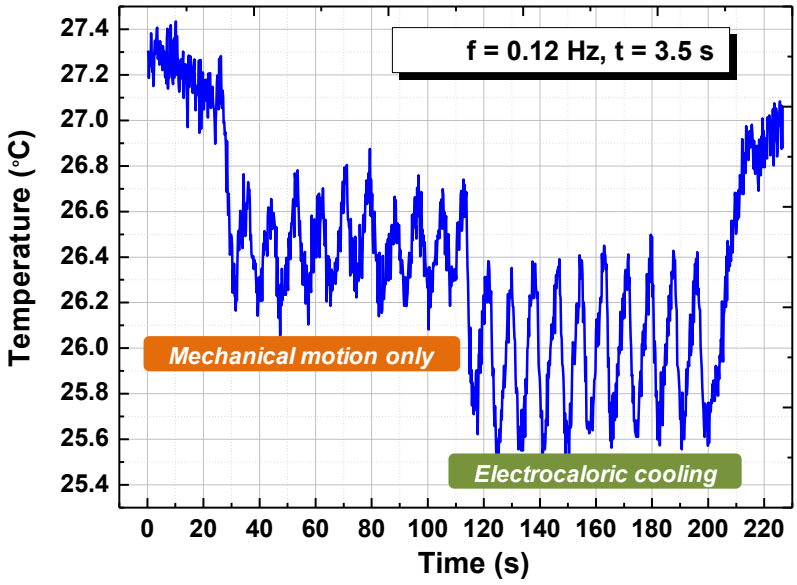
f = 0.12 Hz, t = 3.5 s
Mechanical motion only
Electrocaloric cooling
Temperature (°C)
Time (s)
27.4
27.2
27.0
26.8
26.6
26.4
26.2
26.0
25.8
25.6
25.4
0
20
40
60
80
100
120
140
160
180
200
220

(a)

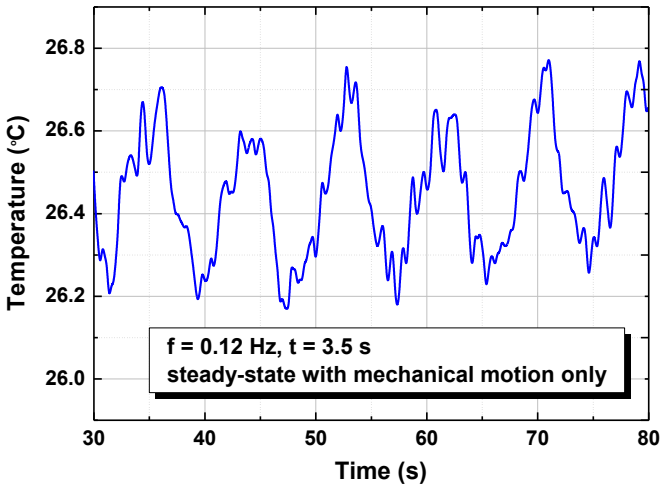
f = 0.12 Hz, t = 3.5 s
steady-state with mechanical motion only
Temperature (°C)
Time (s)
26.8
26.6
26.4
26.2
26.0
30
40
50
60
70
80

(b)

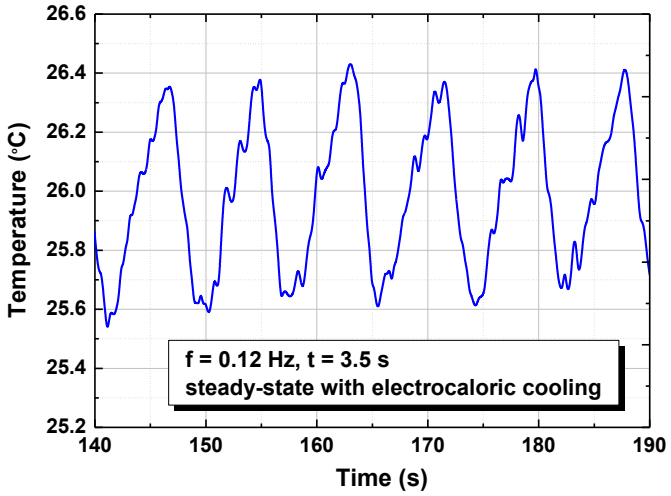

(**c**)

Figure 4.6: (a) The experimentally measured temporal temperature profile of the heater under the initial steady state, under the mechanical oscillation only, and under the electrocaloric cooling conditions. Steady periodic state (b) under the mechanical oscillation only and (c) under the electrocaloric cooling conditions. The cycle frequency is fixed at 0.12Hz.

A transient one-dimensional heat transfer model is constructed to help validate our experimental results. The thin-silicon heater chip is modeled as a lumped thermal mass with a uniform heat source because the Biot number, which is the ratio of the thermal resistance across the chip to that of the liquid thermal interface, is much smaller than 0.1. Transient heat diffusion across the EC material-electrode assembly and the liquid thermal interfaces, whose thicknesses were measured directly from optical images, is modeled using the finite volume method. The electrocaloric heating and cooling effects are

modeled using the quasi adiabatic temperature changes directly measured from a nominally identical capacitor. All other model parameters were taken from the literature and there was no adjustable parameter. The measured transient heater temperature profiles agree well with prediction from the 1D transient heat transfer simulations (Figure 4.7).

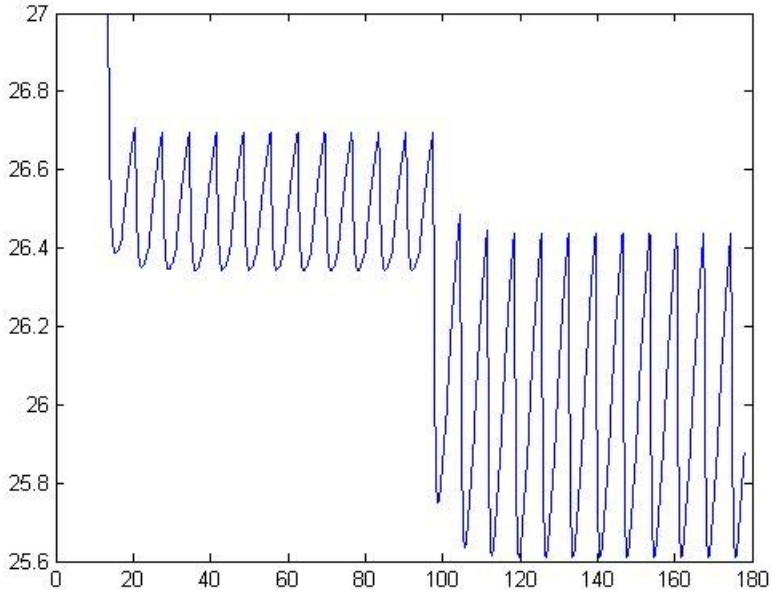

Figure 4.7: The numerically simulated temporal temperature profile of the heater under the initial steady state, under the mechanical oscillation only, and under the electrocaloric cooling conditions. The cycle frequency is 0.12Hz.

4.3.3 Frequency Dependence of the Cooling Performance

To further quantify our experimental results, Figure 4.8(a) shows the cycle-averaged heater temperatures as a function of the cycle frequency. The cycle frequency is varied by changing the residence times of the EC material-electrode assembly on the heater and the heat sink. The mechanical travel time is fixed. The mean temperatures under both the MMO and the EC conditions decrease almost linearly with increasing cycle frequency as more thermal energy is transferred from the heater to the electrocaloric material per unit time.

Figure 4.8(b) shows the difference, ΔT_{mean}, in the cycle-averaged temperature between the MMO and the EC conditions, which is a measure of the net refrigeration capability of the cycle. ΔT_{mean} also increases with increasing cycle frequency over the present measurement range. All the data agree well with the predicted results from the 1D transient thermal modeling.

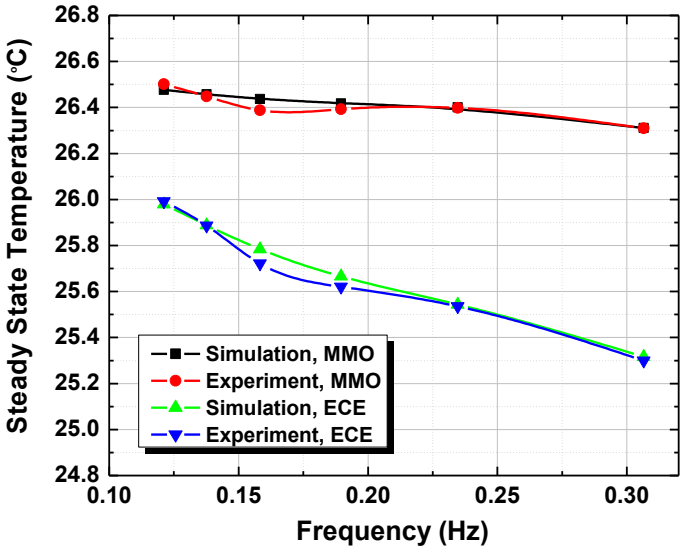

(a)

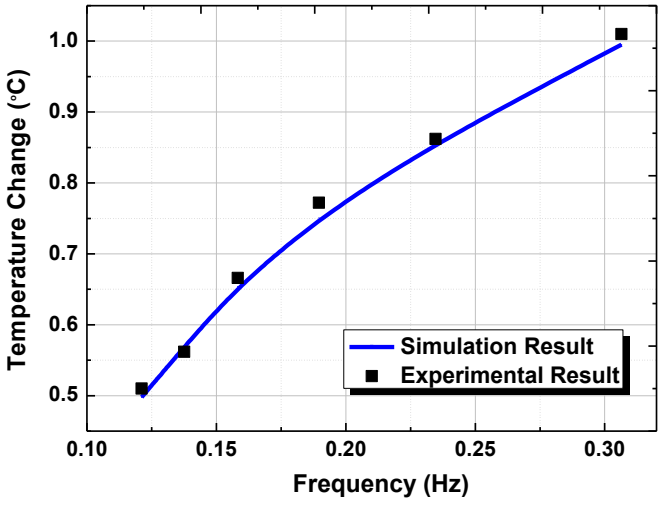

(b)

Figure 4.8: (a) The predicted and measured cycle averaged temperatures under the two steady periodic conditions and (b) their difference as a function of cycling frequency.

In the present experiments, we induce finite Joule heating in the heater (that is, impose a specific cooling load) while characterizing the refrigeration cycle to help reduce complications of parasitic heat transfer to or from the ambient. Under this situation, ΔT_{mean} is a function of the heating power and thermal mass of the heater and should be viewed as a measure of the increased heat transfer rate due to the EC cooling. It may exceed the adiabatic temperature change measured from the stand-alone multi-layer capacitor. The minimum heater temperature may remain higher than the ambient temperature under the specific heater power and some cycle frequencies used in the present experiments.

At the relatively low cycle frequencies we used in the present study, there is sufficient time for "complete" heat transfer between the heat source/sink and the EC material. The cooling energy per cycle is therefore nearly constant. Faster cycling then leads to higher cooling power and hence larger heater temperature drop. However, significant further increase in the cycle frequency (for example, with the use of a microfabricated actuator) may not lead to commensurate increase in ΔT_{mean} due to finite heat diffusion time across the liquid and EC material, the finite thermal mass of the electrode assembly, as well as the diminished driving force ($T_{heater} - T_{EC}$) for heat transfer.

To understand more about the cycle frequency dependence of the cooling performance, the cycle frequency is varied in three different methods. The mechanical travel time is fixed at ~1s. We start from 0.23 Hz (~1.5s residence times of the EC material-electrode assembly on both the top heater surface and the bottom heat sink surface). On one hand, as in the previous discussions, the cycle frequency is decreased by

increasing the residence times on both surfaces by 0.5 s at a time. On the other hand, we can fix the residence time on one surface (~1.5 s) and increase that on the other surface by 1 s at a time to get the same frequency changes. Figure 4.9 shows the mean temperature differences between the MMO and the EC conditions as a function of cycle frequency. By fixing the residence time on the top heater surface and only changing the residence time on the bottom heat sink surface, we can achieve higher temperature changes when the EC condition is turned on.

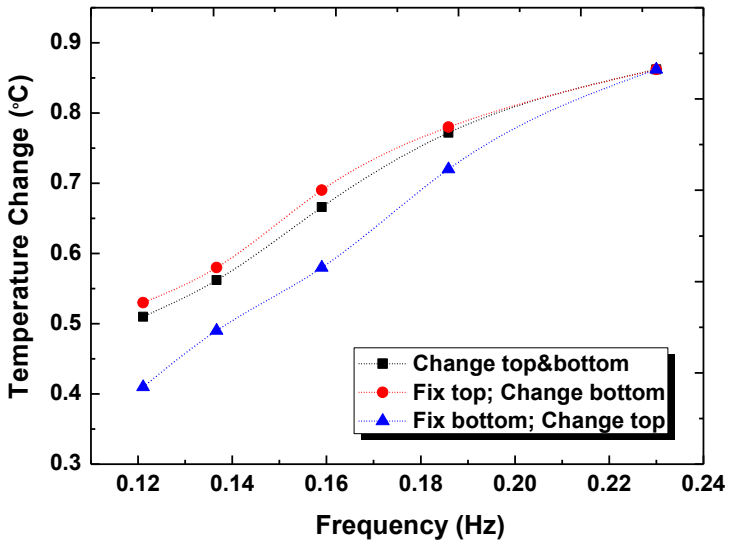

Figure 4.9: Cycle-averaged temperature differences between the MMO and the EC conditions with different frequency varying methods.

4.3.4 Bias Electric Field Dependence of the Cooling Performance

Figure 4.10 shows the difference, ΔT_{mean}, in the cycle-averaged temperature between the MMO and the EC conditions under different bias electric fields for EC materials. ΔT_{mean} also increases with increasing electric fields over the present measurement range, indicating that larger electric fields induce larger electrocaloric effect and hence better cooling performance. However, higher fields may result in irreversible breakdown or dielectric failure in the current EC materials.

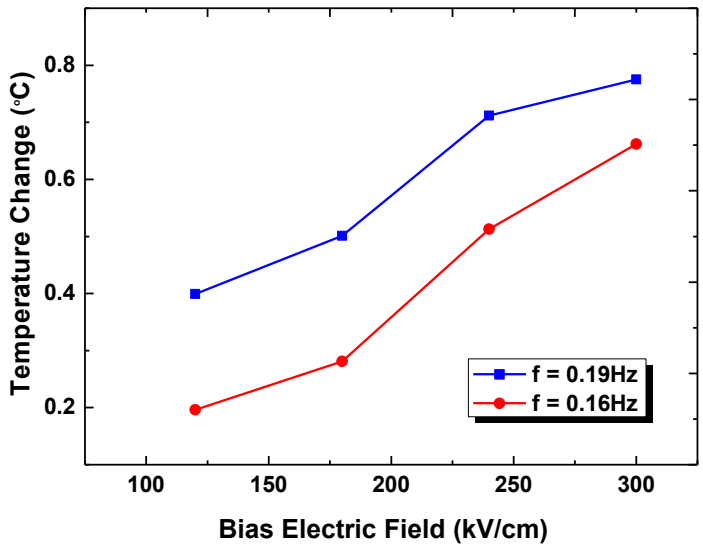

Figure 4.10: Cycle-averaged temperature differences between the MMO and the EC conditions under different bias electric fields.

4.4 Summary

In summary, we report a new design concept for compact solid-state refrigerators based on the electrocaloric (EC) effect. The EC refrigerators are attractive because they may approach the Carnot efficiency more closely than Peltier coolers, which involve intrinsically irreversible processes. To address parasitic losses and other practical considerations that limit the actual performance of EC coolers, we incorporate laterally interdigitated electrode arrays with high effective thermal conductivity and liquid-based switchable thermal interfaces with high switching ratios and high off-state thermal resistance. Direct characterization, as well as numerical simulation, is conducted to quantify the EC effect and the cooling performance. We provide a preliminary demonstration of the device design based on the Y5V multilayer capacitor, which achieves a temperature drop of ~ 1 K at the operating frequency of 0.3 Hz. The present work motivates further experimental studies to exploit advanced electrocaloric materials and optimize the module structure to assess the feasibility of its practical application. Similar to Peltier coolers, multiple modules can be stacked in series to achieve large total ΔT and placed in parallel to achieve high total cooling power.

CHAPTER 5

Direct Electrocaloric Characterization of Thin Films Supported on Substrates

In this chapter, we present a direct thermal characterization of the electrocaloric (EC) heating and cooling in thin films supported on substrates using microfabricated thin-film resistance thermometers. We analyzed the temporal temperature profiles through full three-dimensional heat diffusion modeling and compared results obtained using thin-film thermometers with different temperature coefficients of resistance to assess potential experimental error due to electric or electromagnetic coupling and thereby further validate our approach. Our approach captured asymmetry between the electrocaloric heating and cooling due to hysteresis in the polarization response of P(VDF-TrFE) films and yielded adiabatic temperature changes that agree with existing data.

5.1 Background

The overall cooling performance of the EC refrigerator discussed in the previous chapter is limited by the Y5V multilayer capacitor from three aspects [41]: films of the $BaTiO_3$ compound show small theoretic EC temperature changes (~1 K under ΔE = 100 kV/cm [20]). Large driving field (1000-2000 kV/cm [42]) is not accessible. Doping and the surrounding dielectric suppress phase transitions and therefore EC performance [20, 43].

EC performance can then be significantly improved by better material selection. Replacing the nickel electrodes with materials that have high thermal conductivity and low heat capacity will increase the EC cooling power, hence the temperature drop between the heat load and heat sink. Exploiting the 40 K EC temperature changes measured in 8/65/35 PLZT thin films under 125 MV/m bias field [23], or 7 K in P(VDF-TrFE-CFE) terpolymer films under 100 MV/m [44], will further improve the cooling performance.

To help improve our EC refrigerator performance, in this chapter, we present a characterization approach for the electrocaloric effect (both heating and cooling) in thin EC films as prepared on an insulating substrate. Thin-film resistance thermometers, which double as bottom electrodes, are integrated directly onto the substrate to monitor transient temperature changes in response to the application or removal of electric fields across EC thin films. Such thin-film thermometers can be readily prepared using a single lithography- or shadow mask. The temporal temperature profiles were analyzed using

numerical simulations of heat conduction to help establish the validity of our measurement approach.

5.2 Sample Preparation and Experimental Setup

Figure 5.1 schematically illustrates the cross section of our test structure. A serpentine thin-film thermometer (20 nm Ti/200 nm Au or W) of the overall width of 5 mm was first lithographically defined on a 0.5 mm-thick glass substrate. The thermometer also serves as the bottom electrodes for electrical biasing of an EC thin film deposited on it.

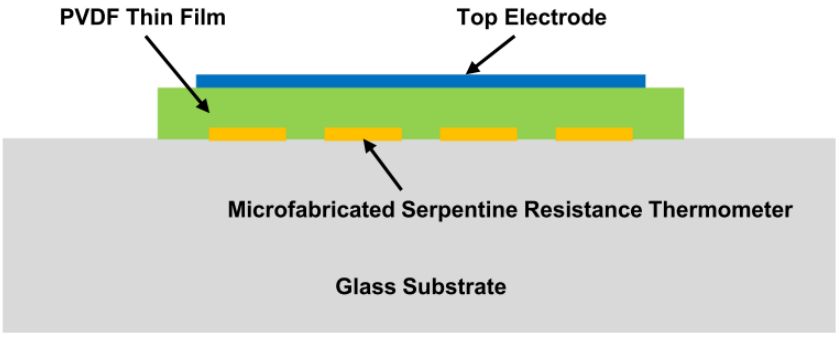

Figure 5.1: Cross section of a characterization sample.

Thin films of a poly(vinylidene fluoride-trifluoroethylene-chlorofluoroethylene) (P(VDF-TrFE-CFE) 56.2:36.3:7.5 mol.%) terpolymer and a poly(vinylidene fluoride-trifluoroethylene) (P(VDF-TrFE) 55/45 mol.%) co-polymer were prepared using a solution-cast method. These polymer types were chosen in part because of the availability of extensive work on similar ter- or co-polymers in the literature and, for the former, in part because of wider temperature ranges accessible to relaxor ferroelectric materials for solid-state EC refrigeration than typical ferroelectric materials. Powders of the ter- or co-polymer were first dissolved in methyl ethyl ketone (MEK) and stirred at 60°C until the powders were completely dissolved. The polymer solution was then filtered using a 0.45 μm-pore size filter and spin coated at 500 rpm on the glass substrates with the prefabricated thin-film thermometers. The samples were subsequently annealed in a vacuum oven at 140–145 °C overnight to evaporate any residual solvent and volatile impurities. Dielectric properties of the films prepared using a similar procedure were characterized and reported in multiple prior publications. The final film thickness was approximately 5 μm. A top electrode was last formed by depositing a 200 nm-thick aluminum film through a shadow mask.

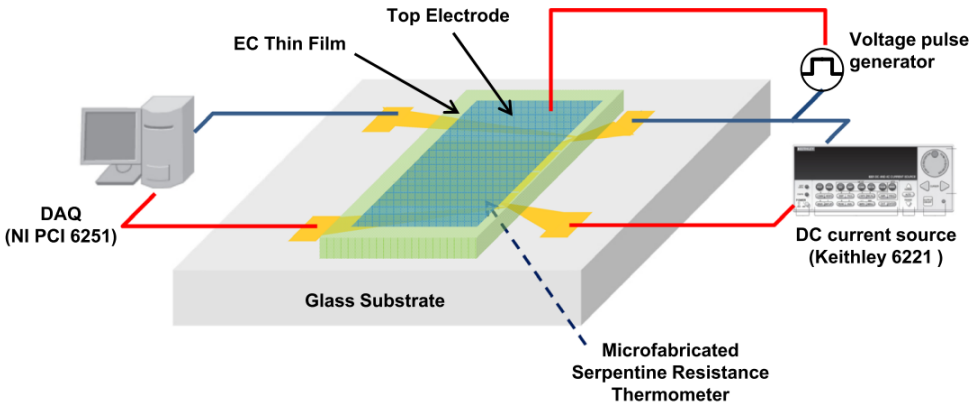

Figure 5.2: The experimental setup used to characterize the electrocaloric effect in thin films.

Figure 5.2 shows an experimental setup used in the present study. A current source (Keithley 6221) was used to apply a DC current of a fixed amplitude to the thin-film resistance thermometer. The resulting voltage drop was monitored using a PC-based analog-to-digital converter (PCI-6251, National Instruments) to obtain the electrical resistance of the thermometer as a function of time. Finite Joule heating in the resistance thermometer allows control of the temperature of the EC films to above the room temperature, approximately 35 °C for the cases reported here. The temperature coefficient of resistance of the thermometer was pre-determined in a separate calibration experiment. The voltage drop across the resistance thermometer was kept below 5 V, approximately two orders of magnitude smaller than the bias voltages applied across the EC films.

5.3 Results and Dicussions

5.3.1 Captured Electrocaloric Cooling and Heating

To induce EC heating or cooling, voltage pulses of varying magnitudes were applied to the top electrode. The rise and fall time of the voltage pulse were measured to be approximately 0.1 ms for all the cases reported in the present chapter. We note that non-rectangular (trapezoidal, triangular, sinusoidal, etc.) electric "pulses" may also be used with our technique. The magnitude of temperature changes and its interpretation, however, are different for different pulse shapes due in part to finite hysteresis in the electric field-polarization relations and in part to a finite timescale associated with thermal diffusion in the substrate.

In the present experiment, the duration of the voltage pulses was fixed at 100 ms, which is much longer than the voltage rise/fall time but is of the same order as the characteristic time for heat diffusion into the substrate. We did not observe any significant change in the temporal temperature profiles even when the pulse duration was increased to 1 s.

Figure 5.3 shows a representative temporal temperature profile obtained in a single voltage pulse sequence using a resistance thermometer made of Au (TCR = 0.003 /K). The EC film first experienced rapid heating and then gradually cooled down to the initial set temperature due to heat diffusion into the substrate. We note that the EC film was

maintained under a quasi-isothermal condition because heat diffusion into the substrate of a much larger thermal mass render the apparent temperature changes in the film much smaller than the true adiabatic values. No significant extra Joule heating caused by a leakage current across the EC film was observed for electric fields up to 110 MV/m. Repeated application of fields greater than that value resulted in irreversible degradation or breakdown of our films. When the bias voltage was removed, the EC film experienced rapid cooling and then gradually warmed up to the initial set temperature.

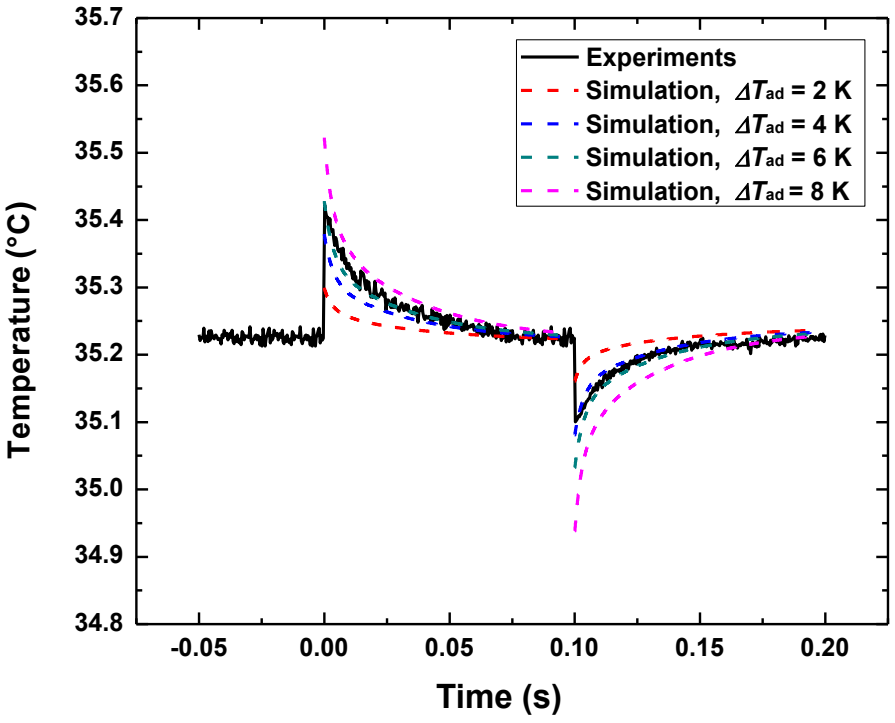

Figure 5.3: The experimentally measured and numerically simulated temporal temperature profiles of the thermometer under the initial steady state, under the bias electric field application, and under the bias electric field removal. The bias electric field is 80 MV/m.

We solved the 3D transient heat diffusion equation using a finite element method to analyze the temporal temperature profiles acquired. The electrocaloric effects were modeled using a uniform volumetric heat source or sink in these simulations. The relevant thermophysical properties of the substrate (thermal conductivity = 1.0 W/m K, heat capacity per unit volume = 1.9 MJ/m^3 K) were independently characterized using the hot disk/wire techniques. The thermal diffusivity ($1x10^{-7}m^2/s$) of the EC film has a relatively small effect because heat diffusion time across the polymer film, approximately 0.25 ms, is much smaller than the characteristic time associated with heat diffusion into the substrate.

Figure 5.3 also shows results from the finite element simulations for different prescribed values of the adiabatic heating or cooling temperatures ΔT_{ad}. The best fit value is considered to represent ΔT_{ad} of the film at that electric field. The simulated temperature profiles qualitatively reproduce the measured profiles very well, strongly suggesting that they indeed represent a thermal phenomenon and not an electrical artifact.

The peak EC heating temperature exceeds the peak EC cooling temperature, resulting in appreciably different temporal temperature profiles around the two switching transitions (field switched on or off). Such "hysteric" behavior was also reported in a calorimetric characterization of P(VDF-TrFE) 65/35 mol % co-polymer samples [45] and a direct characterization of $BaTiO_3$ single crystals [46]. This hysteresis decreases with increasing temperature but at the expense of reduced absolute values of ΔT_{ad} for a given bias field.

5.3.2 Data Validation

To further verify that the measured temperature profiles reflect real thermal phenomena and not experimental artifacts due to electric or electromagnetic coupling, we repeated the measurements using a resistance thermometer made of tungsten with TCR approximately 20 times smaller than that of Au. Figure 5.4 shows the normalized voltage drops obtained from the two different resistance thermometers. The measured changes in the normalized voltage drop (and therefore the relative change in the electrical resistance) scale directly with the measured TCR values. This confirms a negligible experimental error from an electric or electromagnetic coupling that may arise from large swings in the electric field applied across EC thin films.

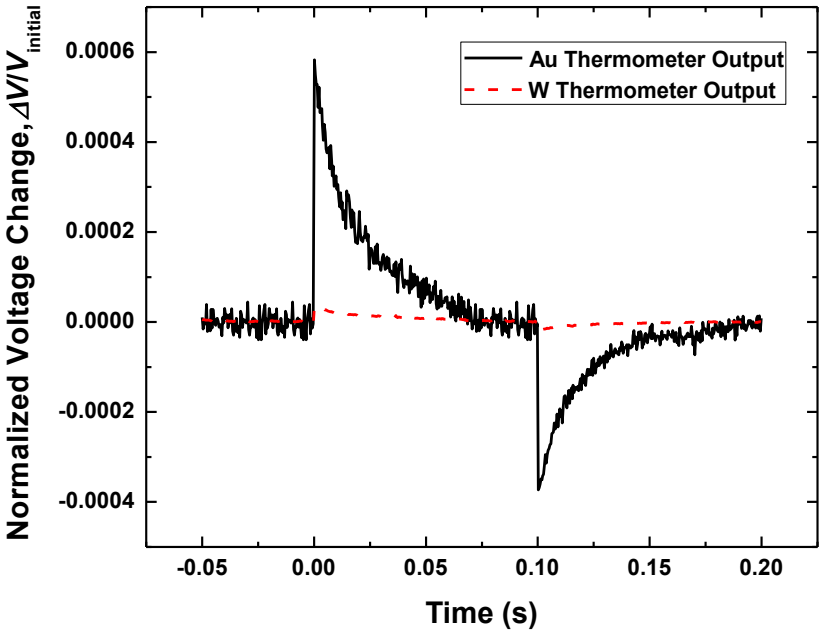

Figure 5.4: Normalized voltage drops across the resistance thermometers with different temperature coefficients of resistance. The bias electric field is also 80 MV/m.

5.3.3 Electric Field Dependence of the EC Effect

Figure 5.5 shows the extracted adiabatic cooling temperatures as a function of the electric field amplitude for the terpolymer films at 35°C. Also plotted for comparison are the values reported in independent previous studies [44, 47] of terpolymer films of similar compositions, which had to be removed from their original substrates for direct or semi-direct characterization. The present data are consistent with the existing data

obtained using a direct method or a calorimetry-based semi-direct method but deviate substantially from the values deduced from the pyroelectric coefficient using Maxwell's relations. The use of Maxwell's relations is known to be problematic for relaxor ferroelectric materials that exhibit non-ergodic behavior.

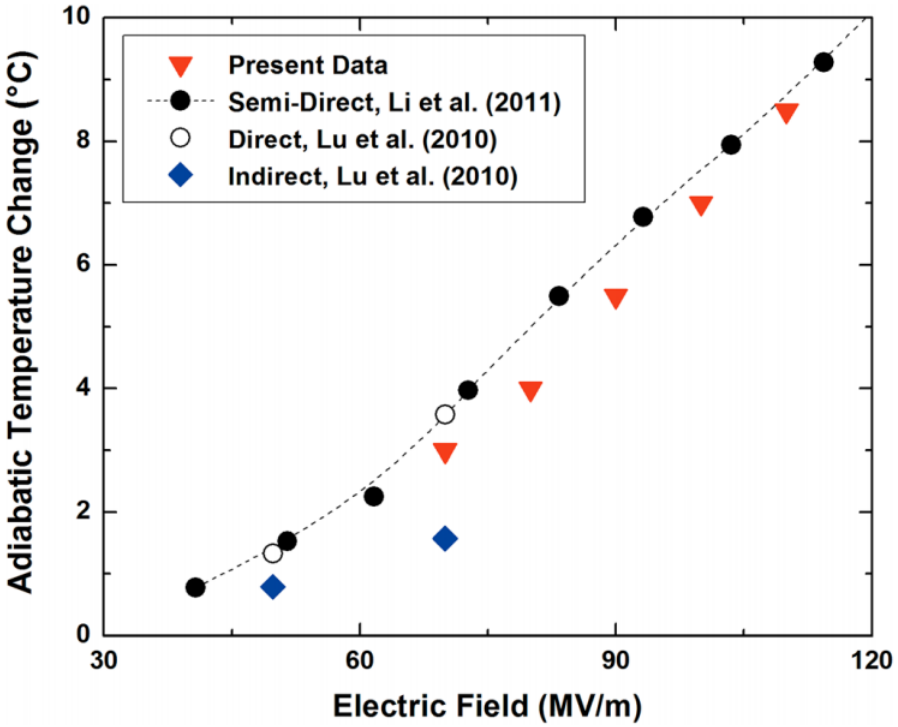

Figure 5.5: Adiabatic EC temperature changes in response to the removal (cool-ing) of an electric field across the EC terpolymer thin film as a function of the electric field amplitude. The values extracted by analyzing the temporal temperature profiles using the 3D heat diffusion analyses are shown as the inverted triangles. Also shown for reference are the values reported in the literature for terpolymer films of similar compositions.

Previous studies, as summarized for example by Valant, suggested the impact of mechanical boundary conditions, thermal stress, and misfit strains on the EC effect in thin ceramic films. For free-standing films, a previous approximate phenomenological model for uniaxial ferroelectrics [48] yielded an expression for the EC-induced entropy change per unit volume,

$$ds^{FS} = -\left[\frac{\beta}{2} + \frac{\alpha\beta(T - T_c)}{2} + \frac{3\alpha\gamma P^2}{4}\right]P^2$$

where β and γ are the coefficients in the Landau-Devonshire phenomenological expansion of the Gibbs free energy and α is the thermal expansion coefficient. The second and the third term represent the secondary electrocaloric effects due to interactions among the thermal expansion, strain, and polarization. These last two terms for the free standing P(VDF-TrFE) samples are estimated to be relatively small, accounting for approximately 25% of the total electrocaloric effect [48].

Similarly, the entropy change for clamped uniaxial ferroelectric films may be approximated as

$$ds^{CF} = -\left[\frac{\beta}{2} + \frac{2\alpha Q_{12}P^2}{(s_{11} + s_{12})}\right]P^2$$

where Q is the electrostrictive coefficient and s is the compliance tensor. The second term in the bracket represents the secondary EC effect for clamped quasi-isothermal samples, reflecting the interplay between thermal expansion and electrostriction to reduce the in-plane strain to zero. The second term is estimated to be approximately 10% of the total

EC effect for the co-polymer samples. The adiabatic temperature changes measured previously from free-standing co-polymer films and those measured from our present experiments agreed also within ~20%, consistent with the above estimates of the secondary EC effects.

5.3.4 Temperature and Sequence Dependence of the EC Effect

Figure 5.6 shows the temporal temperature profiles of the thin-film resistance thermometer at different EC film temperature. As expected for the present terpolymer film, the peak adiabatic temperature change occurs near the curie temperature of around 30 °C [44]. Above this point, higher EC film temperature will induce smaller electrocaloric effect, and hence smaller apparent temperature rise/fall amplitudes in the measurements.

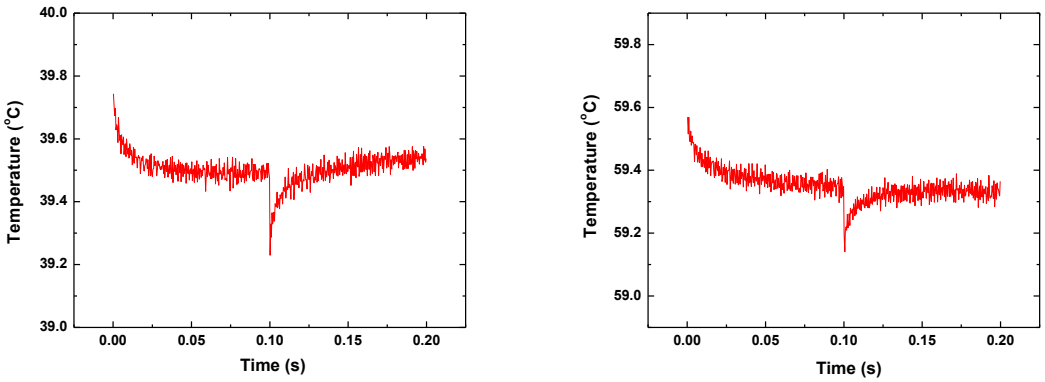

Figure 5.6: The experimentally measured temporal temperature profiles of the thermometer with different substrate temperatures. The bias electric field is 100 MV/m.

For practical refrigeration application, the EC film needs to continuously undergo the cooling cycles. Here, we applied a series of electric pulses to check the temperature response of the EC film. Figure 5.7 shows the temporal temperature profiles corresponding to the first and the fifth pulse. The two profiles are almost identical, and no sequence dependence is captured in the present study.

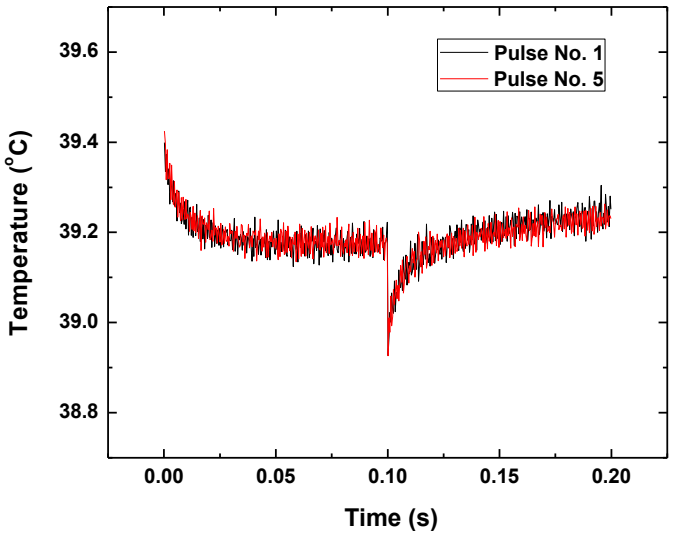

Figure 5.7: Temperature responses to the application and removal of the electric field at different pulse numbers.

5.4 Summary

In summary, the present work reports a direct thermal characterization of EC thin films supported on a substrate. Microfabricated resistance thermometers are directly

integrated onto the substrate to capture changes in the temperature of EC thin films at high temporal resolution while subjecting the EC films to time-varying electric fields. The approach was validated by analyzing the measured temporal temperature profiles using full heat diffusion modeling and by using resistance thermometers made of materials with very different temperature coefficients of resistance. Our experiments captured asymmetry between the electrocaloric heating and cooling due to hysteresis as reported in independent previous studies and matched the adiabatic temperature changes obtained previously from nominally identical films by bonding them on free-standing foils. The present work establishes a versatile and efficient experimental technique to characterize EC thin films on their growth substrates.

CHAPTER 6

Electrocaloric Effect Characterization under AC Electric Field

In this chapter, we discuss a direct characterization of the frequency dependent temperature responses in EC thin films under AC bias electric fields using a high-precision lock-in technique. The temperature responses detected by embedded thin-film resistance thermometers are analyzed using the steady periodic solutions of a 3D heat conduction model to extract the equivalent volumetric heat sources, corresponding respectively to the electrocaloric effects and hysteresis losses. The bias filed frequency and amplitude dependence of the heat sources agrees well with our model predictions, and the volumetric heating rates due to the hysteresis losses are estimated to be as much as 15% of the EC heating/cooling rates for the EC material studied here. The extracted values of the loss tangent and adiabatic EC temperature change are also consistent with the independently measure data.

6.1 Background

Previous studies, including our own [49], reported that measured temperature rises due to EC heating very often exceeded measured temperature drops due to EC cooling. This resulted in asymmetric temperature profiles over the two switching transitions (electric field switched on or off). Such "hysteric" behavior was also observed in a calorimetric characterization of polymeric EC samples and in a direct characterization of the adiabatic temperature changes in $BaTiO_3$ single crystals. A more recent study [50] reported observation of a potential impact of the hysteresis loss in their measurements of long-term temperature rises in an EC material subjected to periodic electric pulses. Detailed and direct thermal and electrical analyses of the hysteresis loss, however, were not presented.

The hysteresis loss, if significant, can degrade the coefficient of performance of EC refrigerators and hinder their practical implementations. Systematic studies of the hysteresis effect in EC materials during polarization switching, however, have so far been lacking.

In the present work, we study a direct characterization of the frequency dependence temperature responses in EC thin films under AC bias electric fields. The temperature responses were detected using embedded thin-film resistance thermometers in conjunction with a high-precision lock-in technique. The results are analyzed using the steady periodic solutions of a 3D heat conduction model. Equivalent volumetric heat sources corresponding respectively to reversible electrocaloric effects and irreversible

hysteresis losses were extracted as a function of the frequency and amplitude of sinusoidal bias electric fields to deduce the potential impact and parametric dependence of the EC effects and the hysteresis loss.

6.2 Sample Preparation and Experimental Setup

A serpentine thin-film thermometer (20 nm Ti/200 nm Au or W) of the overall width of 5 mm was first lithographically defined on a 0.5 mm-thick glass substrate. The thermometer also serves as the bottom electrodes for electrical biasing of an EC thin film deposited on it. Thin films of a poly(vinylidene fluoride-trifluoroethylene-chlorofluoroethylene) (P(VDF-TrFE-CFE) 56.2:36.3:7.5 mol %) terpolymer were prepared on the substrate using a solution-cast method. Details of the test structure and sample preparation procedures were reported in our prior publication[6] and will not be repeated here.

Figure 6.1 shows the experimental setup used in the present study. A current source (Keithley 6221) was used to apply a DC current of a fixed amplitude (1 mA) to the thin-film resistance thermometer. Sinusoidal voltages of different amplitudes and frequencies were applied to the top electrode to induce the EC effects in the thin film. The changes in the voltage drop across the resistance thermometer and hence its temperature oscillations were monitored using a lock-in amplifier (Stanford SR830). The temperature coefficient of the resistance thermometer was pre-calibrated in an independent experiment. The frequency range of the applied sinusoidal EC bias field was set below 250 Hz (or main

EC heating/cooling frequency of 500 Hz) in consideration of the finite heat diffusion time across the polymer film (~3 μm). The amplitudes of EC bias electric fields were set below 40 MV/m. Application of higher fields often resulted in irreversible degradation or breakdown of our films.

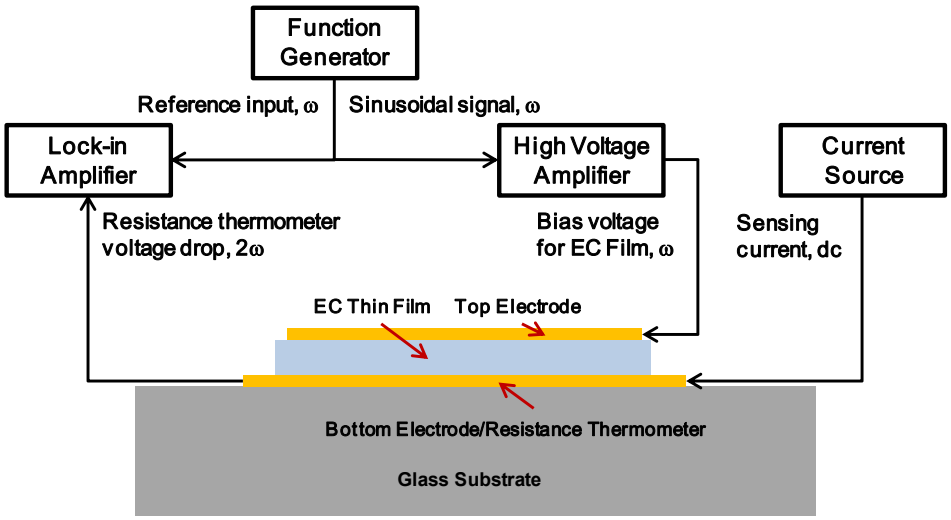

Figure 6.1: The experimental setup used to characterize the electrocaloric effects and hysteresis loss in EC films supported on a glass substrate under sinusoidal bias electric fields.

One can in principle characterize time- or frequency-dependence of the EC effects and hysteresis losses by applying voltage pulses of varying rise and fall times across EC materials. The lock-in technique, however, very often allows more precise measurements of temperature changes, which is an important advantage for characterizing thin films

that are supported on and hence in intimate thermal contact with the substrates at moderate amplitudes of bias electric fields.

6.3 Results and Discussions

6.3.1 Experimental Data and Modeling Results

We numerically solved the 3D transient heat conduction equation under the steady-periodic assumption (Eq. 6.1-6.3) to analyze the measured temperature oscillations. A matching equation without the heat source term was solved simultaneously for the glass substrate. For a sinusoidal bias electric field at angular frequency ω, we focus on the volumetric heat source at angular frequency 2ω because the EC effects and hysteresis losses were not expected to be polarity dependent in our relaxor ferroelectric films.

$$0 = k_{EC}\left(\frac{\partial^2 \tilde{T}_{EC}}{\partial x^2} + \frac{\partial^2 \tilde{T}_{EC}}{\partial y^2} + \frac{\partial^2 \tilde{T}_{EC}}{\partial z^2}\right) + i \cdot 2\omega \cdot \left(-\rho c_p \tilde{T}_{EC}\right) + q''' \tag{6.1}$$

$$E = E_0 e^{i\omega t} \tag{6.2}$$

$$T_{EC} = \tilde{T}_{EC} e^{i2\omega t} + T_0 \tag{6.3}$$

here ρ_{EC}, c_{EC}, and T_{EC} are the density, specific heat and temperature of the EC thin film, respectively, and are assumed to be constant. T_0 is the DC temperature of the EC film. E

is the electric field applied to the EC thin film with E_0 being its amplitude of and ω being its angular frequency.

The volumetric heat source q''' is modeled to consist of q_{EC}''' due to the electrocaloric effects and q_{H}''' due to the hysteresis loss.

$$q''' = q_H''' + q_{EC}''' \tag{6.4}$$

The volumetric heat source q_{EC}''' represents the EC heating and cooling effects. The amount of thermal energy released or absorbed due to EC heating/cooling effect is approximately proportional to E^2 or $(E_0 \mathrm{e}^{\mathrm{i}\omega t})^2$. By taking the first order time derivative of this term, we write

$$q_{EC}''' = i \cdot \omega \rho_{EC} c_{p_{EC}} \Delta T_{ad} e^{i2\omega t} \tag{6.5}$$

We expressed the proportionality factor in terms of ΔT_{ad}, which is the adiabatic temperature change for a given amplitude of the bias electric field, to facilitate comparison with the existing data obtained by applying pulsed bias fields to EC materials.

When an external electric field is applied to reverse the polarization of an EC material, one consequence of accompanying domain wall motions or switching is the occurrence of the hysteresis loop [51]. Resistance to these motions causes losses, which

in turn leads to volumetric heating [52]. These losses may be described using the dielectric loss parameter ε'', an imaginary part of the material's complex permittivity ε:

$$\varepsilon = \varepsilon_0(\varepsilon' - i\varepsilon'') \tag{6.6}$$

here ε_0 is the permittivity of free space (ε_0 = 8.86 x 10^{-12} F/m) and the real part ε' is the relative dielectric constant. The loss tangent is defined as

$$\tan\delta = \frac{\varepsilon''}{\varepsilon'} = \frac{\sigma}{\omega\varepsilon_0\varepsilon'} \tag{6.7}$$

here σ is the total effective conductivity (S/m). The volumetric heating rate due to the hysteresis loss is then expressed as

$$q_H''' = \sigma E^2 = \omega\varepsilon_0\varepsilon' \tan\delta \cdot E_0^2 e^{i2\omega t} = \gamma\omega e^{i2\omega t} \tag{6.8}$$

here, we call γ the frequency coefficient for the hysteresis loss term. For a constant value of the loss tangent tan δ, the coefficient γ would be proportional to the square of the bias electric field amplitude.

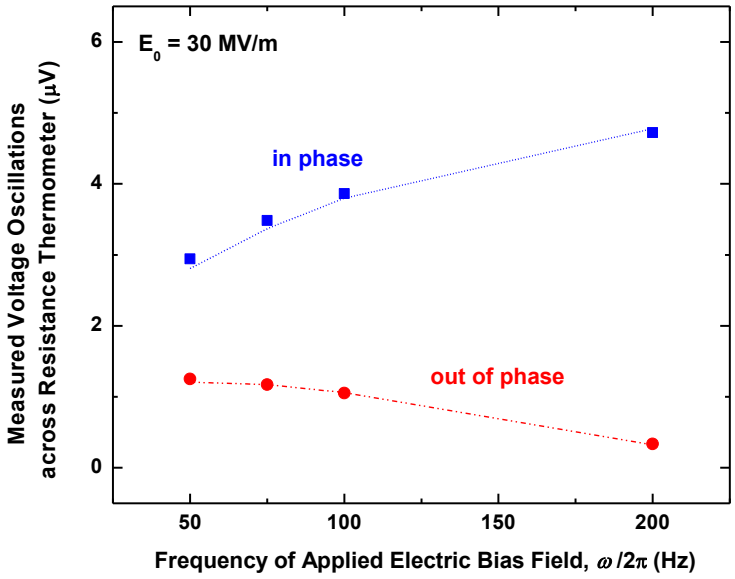

Figure 6.2: In phase and out of phase components of the voltage oscillations across the thin film resistance thermometer. The DC sensing current applied to the resistance thermometers was fixed at 1 mA. The voltage oscillations across the resistance thermometer reflect temperature changes due to the electrocaloric effects and hysteresis loss. The symbols are the experimental data and the lines are the values predicted using the model discussed in the text.

Figure 6.2 shows the measured amplitudes of the in- and out of phase components of the second harmonic voltage across the resistance thermometer. The amplitude of applied EC bias electric fields was 30 MV/m. Also shown for comparison are the amplitudes predicted using the relative dielectric constant, loss tangent, and adiabatic temperature change of the EC film independently determined from nominally identical

films. The predicted frequency dependence of the thermometer voltage oscillations reproduced the experimental data reasonably well.

6.3.2 Frequency Dependence of the Volumetric Heat Sources

Figure 6.3 shows the extracted amplitudes of the volumetric heat source term as a function of the frequency of the bias electric field applied across the EC film. In Eq. 6.4-6.5 and 6.8, the real part of the volumetric heat source term corresponds to the hysteresis losses and the imaginary part corresponds to the EC effects. The observed linear frequency dependence of q_{EC}''' suggests that there is no appreciable effect of the bias field frequency on the adiabatic temperature change at least at frequencies below 200 Hz. Comparing the real and imaginary parts, we estimate that the volumetric heating rates due to the hysteresis losses can be as much as 15% of the EC heating/cooling rates for the EC material studied here.

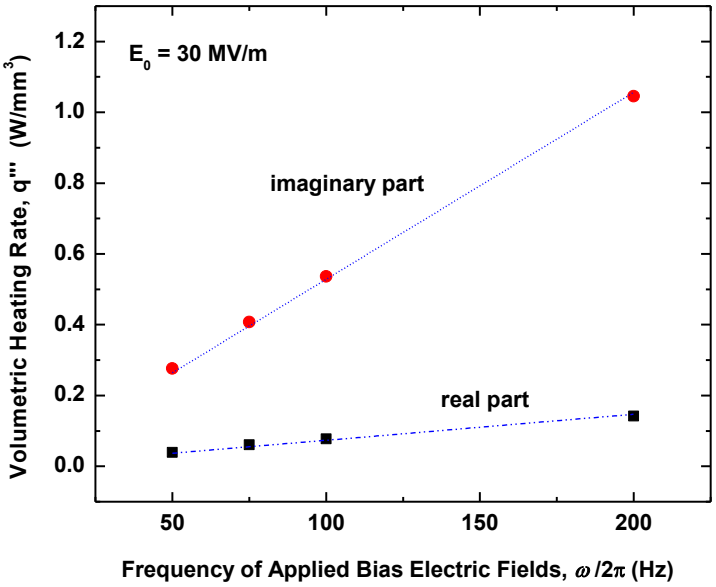

Figure 6.3: Frequency dependence of the real and imaginary parts of the volumetric heating rate. The values were extracted by analyzing the measured temperature oscillations using the steady periodic solutions of the 3D heat conduction model. The lines are linear fits to the data.

6.3.3 Electric Field Dependence of the Hysteresis Loss

We next repeated the measurements and analyses for different values of the amplitude of bias electric fields, E_0. Figure 6.4 shows the extracted frequency coefficient γ (that is, the slope of the linear fit to the real part shown in Figure 6.3) for the hysteresis loss term as a function of E_0^2. Referring back to Eq. 6.8, the linear relationship between γ and E_0

suggests that term $\varepsilon' \tan\delta$ remains nearly constant within the field amplitude range studied here.

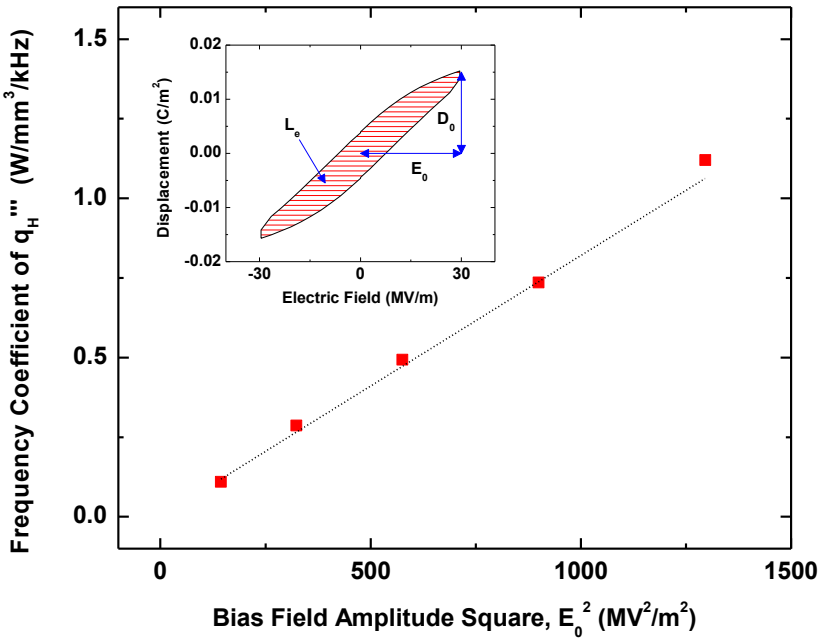

Figure 6.4: Experimentally determined values of the frequency coefficient, γ, of the real part of the volumetric heat source (q_H''') as a function of the square of the amplitude of the applied bias fields, E_0^2. Shown as a guide is the linear fit to the experimental values. The inset shows the independently measured hysteresis loop.

This field amplitude dependence and the extracted value of the loss tangent (~ 0.26) all agree with our independent measurements of the loss factor from the polarization –

electric field hysteresis curves. One such curve is shown in the inset of Figure 6.4. The effective loss tangent could be calculated as [53]

$$\tan\delta = \tan\left[\sin^{-1}\left(\frac{L_e}{\pi D_0 E_0}\right)\right] \quad . \tag{6.9}$$

here D_0 is the amplitude of the electric displacement, and L_e is the hysteresis loop area.

6.3.4 Electric Field Dependence of the EC Effect

The adiabatic temperature changes of the EC film under different bias field amplitudes were similarly calculated using Eq. 6.5 from the frequency coefficients of q_{EC}''', that is, the slopes of linear fits to the imaginary part of the measured volumetric heating rates (e.g., data shown in Figure 6.3). Figure 6.5 shows the extracted adiabatic EC temperature changes as a function of the electric field amplitude. Also plotted for comparison were the values reported in previous studies [49] for terpolymer films of the nominally identical composition. The present values agree well with the previous data within experimental uncertainties.

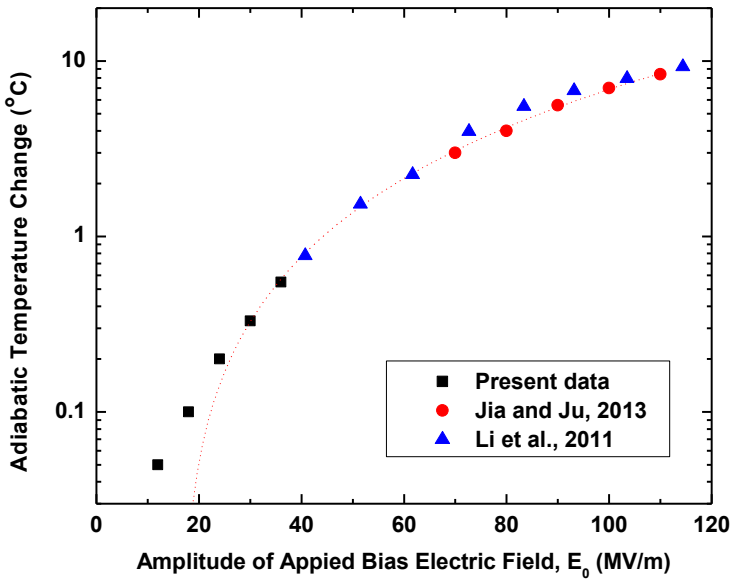

Figure 6.5: Experimentally determined adiabatic temperature changes as a function of the applied bias field amplitude. Also shown for comparison are the values independently obtained from direct measurements of the temperature changes in EC films of a nominally identical composition. The line is a polynomial fit ($C_1 E + C_2 E^2$) to serve as a guide to the eye.

6.4 Summary

In summary, the present work reports a direct characterization of the frequency dependent temperature responses in EC thin films under AC bias electric fields. The lock-in technique provides a high resolution measurement of the resulting voltage changes across the embedded thin-film resistance thermometers to capture more precise

temperature responses. The results are analyzed using the steady periodic solutions of a 3D heat conduction model. The bias filed frequency and amplitude dependence of the equivalent volumetric heat sources, corresponding respectively to the electrocaloric effects and hysteresis losses, agrees well with our model predictions, and the extracted values of the loss tangent and adiabatic EC temperature change are consistent with the independently measured data. The volumetric heating rates due to the hysteresis losses are estimated to be as much as 15% of the EC heating/cooling rates for the EC material studied here. The present work also establishes a fast and efficient experimental technique to allow further studies of other thermal or mechanical impacts on EC effects in thin films.

CHAPTER 7

Summary and Recommendations

The present work demonstrates a new device concept of a compact solid-state cooling module based on the giant electrocaloric effect. Our novel design realizes controllable thermodynamic cycles for the ferroelectric material thin films with laterally interdigitated electrodes. It also exploits the liquid-based thermal interfaces to enable reliable and high-contrast thermal switching and at the same time offer high off-state resistance to minimize deleterious parasitic heat transfer.

We extensively study liquid-based switchable thermal interfaces to circumvent the drawbacks of current designs and fulfill the requirements of practical applications. We design and characterize a switchable thermal interface based on an array of discrete liquid droplets to decrease the mechanical stroke for switching, and a solid-liquid hybrid interface based on an array of micromachined metal posts to significantly enhance heat conduction in the on-state, in turn to reduce the required loading pressure.

We numerically and experimentally characterize the cooling performance of our novel EC refrigerator, and find the limitations of our current EC materials. We then develop two new direct methods to investigate the EC effects in thin films. One is to measure the temporal temperature profiles of EC thin films on substrates using an embedded thin-film resistance thermometer. The other is to capture the frequency dependent temperature responses in EC thin films under AC electric fields using a high-precision lock-in technique.

The following recommendations are made for future research on EC refrigerators and EC characterizations.

EC cooling performance can be significantly improved by better material selection, such as electrode materials that have high thermal conductivity and low heat capacity, and organic or inorganic relaxor ferroelectric materials that have high EC temperature changes. Moreover, it is widely accepted that the EC cooling effect is expected to be most effective around the Curie temperature, where the material undergoes the transition between ferroelectric and paraelectric phases. By tailoring the Curie temperature near the refrigerator working condition, the cooling power can be optimized.

The laterally interdigitated array or the multilayer capacitor structure can compensate the small thermal mass and slow heat diffusion of EC thin films, and an optimal design can be developed based on the thermalphysical properties of the selected materials. Similar to Peltier coolers, multiple modules can be stacked in series to achieve large total ΔT and placed in parallel to achieve high total cooling power.

The EC characterization methods mentioned in the present work are both based on the EC thin films as prepared or clamped on an insulating substrate. The large thermal mass of the substrate render the apparent temperature changes in the film much smaller than the true adiabatic values. One can prepare free-standing EC films or use ultra-thin substrates such as nanoscale SiN_x membranes for more significant temperature signals and more precise measurements. One can also perform circuit-level design to increase the signal-to-noise ratio, and hence the resolution and accuracy of the experiments.

References

[1] Song, W, Sutton, M. S., and Talghader J. J., "Thermal contact conductance of actuated interfaces," Applied Physics Letters, Vol. 81, 2002, 1216-1218

[2] Cho, J. , Richards, C., Bahr, D., Jiao, J., and Richards, R., Journal of Micromechanics and Microengineering, Vol. 18, 2008, 105012

[3] Eriksson, P., Andersson, J.Y., Stemme, G., "Thermal characterization of surface-micromachined silicon nitride membranes for thermal infrared detectors", Journal of Microelectromechanical Systems, Vol.6, 1997, pp.55-61

[4] Laws, A., Chang, R. Y., Bright, V. M., and Lee, Y. C., "Thermal conduction switch for thermal management for chip-scale atomic clocks", Journal of Electronic Packaging, Vol. 130,2008, 021011-1-021011-6

[5] Ghoshal, U., Ghoshal, S., McDowell, C., Shi, L., Cordes, S. and Farinelli, M., "Enhanced thermoelectric cooling at cold junction interfaces," Applied Physics Letters Vol. 80, 2002, 3006-3008

[6] Biter, W., Oh, S., and Hess, S., "Electrostatic Switched Radiator for Space Based Thermal Control," In proceedings of STAIF-2002, Vol. 608, 2002, pp. 73-80

[7] Cha, G., and Ju, Y. S., "Pyroelectric Energy Harvesting using Liquid-Based Switchable Thermal Interfaces," Sensors Actuators Physics, Vol. 89, 2013, pp. 100-107

[8] Jia, Y., and Ju, Y.S., ″A solid-state refrigerator based on the electrocaloric effect," Applied Physics Letters, Vol. 100, 2012, 242901

[9] Miner, A. and Majumdara, A., Ghoshal, U.,"Thermoelectromechanical refrigeration based on transient thermoelectric effects", Applied Physics Letters Vol. 75, 1999, pp. 1176-1178

[10] Cha, G., Jia, Y., Ju, Y. S., "High power density pyroelectric energy harvesting using microfabricated liquid-based thermal switches", In Proceedings of IEEE Conference *MEMS* 2012, Paris, France

[11] Xu, J., and Fisher, T.S., "Enhancement of thermal interface materials with carbon nanotube arrays," International Journal of Heat and Mass Transfer, Vol. 49, 2006, pp. 1658-1666

[12] Ngo, Q., Cruden, B.A., Cassell, A.M., Sims, G., Meyyappan, M., Li, J., and Yang, C.Y., "Thermal interface properties of Cu-filled vertically aligned carbon nanofiber arrays," Nano Letter, Vol. 4, 2004, pp. 2403–2407

[13] Zhao, Y., Tong, T., Delzeit, L., Kashani, A., Meyyapan, M., and Majumdar, A., "Interfacial energy and strength of multiwalled-carbon-nanotube-based dry adhesive," J. Vac. Sci. Technol. B, Vol. 24, 2006, pp. 331:1–331:5

[14] Cha, G., and Ju, Y. S., "Reversible thermal interfaces based on microscale dielectric liquid layers," Applied Physics Letters, Vol. 94, 2009, 211904

[15] M. Valant, "Electrocaloric materials for future solid-state refrigeration technologies," Progress in Materials Science, Vol. 57, 2012, pp. 980

[16] Ju, Y.S., "Solid-state refrigeration based on the Electrocaloric effect for electronics cooling, " Journal of Electronic Packaging, Vol. 130, 2010, 041004

[17] Scott, J. F., "Electrocaloric materials," Annual Review of Materials Research, Vol. 41, 2011, pp. 229-240

[18] Lu, S. G., and Zhang, Q. M., "Electrocaloric materials for solid-state refrigeration," Advanced Materials, Vol. 21, 2009, pp. 1983-1987

[19] Lu, S. G., Rožič, B., Kutnjak, Z., and Zhang, Q.M., "Electrocaloric effect (ECE) in ferroelectric polymer films", Ferroelectrics, Dr Indrani Coondoo (Ed.)

[20] Akcay, G., Alpay, S. P., Mantese, J. V., and Rossetti Jr., G. A., "Magnitude of the intrinsic electrocaloric effect in ferroelectric perovskite thin films at high electric fields," Applied Physics Letters, Vol. 90, 2007, 252909

[21] Bai, Y., Zheng, G., and Shi, S., "Direct measurement of giant electrocaloric effect in $BaTiO_3$ multilayer thick film structure beyond theoretical prediction," Applied Physics Letters, Vol. 96, 2010, 192902

[22] Sebald, G., Seveyrat, L., Capsal, J.-F., Cottinet, P.-J., and Guyomar, D., "Differential scanning calorimeter and infrared imaging for electrocaloric characterization of poly(vinylidene fluoride-trifluoroethylene-chlorofluoroethylene) terpolymer," Applied Physics Letters, Vol. 101, 2012, 022907

[23] Lu, S.G., Rožič, B., Zhang, Q.M., Kutnjak, Z., Li, X., Furman, E., Gorny, L.J., Lin, M., Malič, B., Kosec, M., Blinc, R., and Pirc, R., "Organic and inorganic relaxor ferroelectrics with giant electrocaloric effect," Applied Physics Letters, Vol. 97, 2010, 162904

[24] Kar-Narayan, S., Crossley, S., Moya, X., Kovacova, V., Abergel, J., Bontempi, A., Baier, N., Defay, E., and Mathur, N.D., "Direct electrocaloric measurements of a multilayer capacitor using scanning thermal microscopy and infra-red imaging," Applied Physics Letters, Vol. 102, 2013, 032903

[25] Mischenko, A. S., Zhang, Q., Scott, J. F., Whatmore, R. W., and Mathur, N. D., "Giant electrocaloric effect in thin-film $PbZr_{0.95}Ti_{0.05}O_3$," Science, Vol. 311, 2006, pp. 1270-1271

[26] Chu, B., Zhou, X., Ren, K., Neese, B., Lin, M., Wang, Q., Bauer, F., Zhang, Q. M., "A dielectric polymer with high electric energy density and fast discharge speed," Science, Vol. 313, 2006, pp. 334-336

[27] Sinyavsky,Y. V., and Brodyansky,V. M., "Experimental testing of electrocaloric cooling with transparent ferroelectric ceramic as a working body," Ferroelectrics, Vol. 131, 1992, pp. 321

[28] Mischenko, A. S., Zhang, Q., Whatmore, R. W., Scott, J. F., and Mathur, N. D., "Giant electrocaloric effect in the thin film relaxor ferroelectric 0.9 $PbMg_{1/3}Nb_{2/3}O_3$ - 0.1 $PbTiO_3$ near room temperature," Applied Physics Letters, Vol. 89, 2006, 242912

[29] Kar-Narayan, S., and Mathur, N. D., "Predicted cooling powers for multilayer capacitors based on various electrocaloric and electrode materials," Applied Physics Letters, Vol. 95, 2009, 242903

[30] Epstein, R. I., and Malloy, K. J., "Electrocaloric devices based on thin-film heat switches," Journal of Applied Physics, Vol. 106, 2009, 064509

[31] de Souza, E.J., Brinkmann, M., Mohrdieck, C., and Arzt, E., “Enhancement of capillary forces by multiple liquid bridges,” Langmuir, Vol. 24, 2008, pp. 8813–8820.

[32] de Souza, E.J., Brinkmann, M., Mohrdieck, C., Crosby, A., and Arzt, E., “Capillary forces between chemically different substrates,” Langmuir, Vol. 24, 2008, pp. 10161–10168

[33] Valkenburg, M.E.V., Vaughn, R.L., Williams, M., and Wilkes, J.S., “Thermochemistry of ionic liquid heat-transfer fluids,” Thermochimica Acta, Vol. 425, 2005, pp. 181–188

[34] Swatloski, R.P., Holbrey, J.D., and Rogers, R.D., “Ionic liquids are not always green: Hydrolysis of 1-butyl-3-methylimidazolium hexafluorophosphate,” Green Chemistry, Vol. 5, 2003, pp. 361–363

[35] Jia, Y., Cha, G., and Ju, Y. S., “Switchable thermal interfaces based on discrete liquid droplets,” Micromachines, Vol. 3, 2012, pp. 10–20

[36] Nam, Y., Sharratt, S., Byon, C., Kim, S. J., and Ju, Y. S., “Fabrication and characterization of the capillary performance of superhydrophilic Cu micropost arrays,” Journal of Microelectromechanical Systems, Vol. 19, 2010, pp. 581 –588

[37] Bulgrin, K. E., Ju, Y. S., Carman, G. P., and Lavine, A. S., “An Investigation of a tunable magnetomechanical thermal switch,” Journal of Heat Transfer, Vol. 133, 2011, pp. 101401

[38] Jia, Y., and Ju, Y. S., “Solid-liquid hybrid thermal interfaces for low-contact pressure thermal switching,” Journal of Heat Transfer, Vol. 136, 2014, pp. 074503

[39] Olsen,R. B., Bruno, D. A., Briscoe, J. M., and Jacobs, E. W., “Pyroelectric conversion cycle of vinylidene fluoride-trifluoroethyelene copolymer”, Journal of Applied Physics, Vol. 57, 1985, pp. 5036-5042

[40] Sebald, G., Lefeuvre, E., and Guyomar, D., “Pyroelectric energy conversion: optimization principles”, IEEE Trans. Ultrason. Ferroelectr. Freq. Control, Vol. 55, 2008, pp. 538-551

[41] Kar-Narayan, S., and Mathur, N. D., "Direct and indirect electrocaloric measurements using multilayer capacitors," Journal of Physics D: Applied Physics, Vol. 43, 2010, 032002

[42] Neese, B., Chu, B., Lu, S. G., Wang, Y., Furman, E., and Zhang, Q. M., "Large electrocaloric effect in ferroelectric polymers near room temperature," Science, Vol. 321, 2008, pp. 821

[43] Akcay, G., Alpay, S. P., Rossetti Jr., G. A., and Scott, J. F., "Influence of mechanical boundary conditions on the electrocaloric properties of ferroelectric thin films," Journal of Applied Physics, Vol. 103, 2008, 024104

[44] Li, X., Qian, X., Lu, S. G., Cheng, J. P., Fang, Z., and Zhang, Q. M., "Tunable temperature dependence of electrocaloric effect in ferroelectric relaxor poly(vinylidene fluoride-trifluoroethylene-chlorofluoroethylene terpolymer," Applied Physics Letters, Vol. 99, 2011, 052907

[45] Li, X., Qian, X., Gu, H., Chen, X., Lu, S.G., Lin, M., Bateman, F., and Zhang, Q.M., "Giant electrocaloric effect in ferroelectric poly(vinylidenefluoride-trifluoroethylene) copolymers near a first-order ferroelectric transition," Applied Physics Letters, Vol. 101, 2012, 132903

[46] Moya, X., Stern-Taulats, E., Crossley, S., González-Alonso, D., Kar-Narayan, S., Planes, A., Mañosa, L., and Mathur, N.D., "Giant electrocaloric strength in single-crystal $BaTiO_3$," Advanced Materials, Vol. 25, 2013, pp. 1360

[47] Lu, S.G., Rožič, B., Zhang, Q.M., Kutnjak, Z., Pirc, R., Lin, M., Li, X., and Gorny, L., "Comparison of directly and indirectly measured electrocaloric effect in relaxor ferroelectric polymers," Applied Physics Letters **97**, 2010, 202901

[48] Lu, S.G., Rožič, B., Zhang, Q.M., Kutnjak, Z., and Pirc, R., "Electrocaloric effect in ferroelectric polymers," Applied Physics A, Vol. 107, 2012, pp. 559-566

[49] Jia, Y., and Ju, Y. S., "Direct characterization of the electrocaloric effects in thin films supported on substrates," Applied Physics Letters, Vol. 103, 2013, 042903

[50] Gu, H., Qian, X., Li, X., Craven, B., Zhu, W., Cheng, A., Yao, S. C., and Zhang, Q. M., "A chip scale electrocaloric effect based cooling device," Applied Physics Letters, Vol. 102, 2013, 122904

[51] Damjanovic, D., "Ferroelectric, dielectric and piezoelectric properties of ferroelectric thin films and ceramics," Reports on Progress in Physics, Vol. 61, 1998, pp. 1267

[52] Clark, D. E., and Sutton, W. H., "Microwave processing of materials," Annual Review of Materials Science, Vol. 26, 1996, pp. 299-331

[53] Gallagher, J. A., Jo, H. R., and Lynch, C. S., "Large-field dielectric loss in relaxor ferroelectric PLZT," Smart Materials and Structures, Vol. 23, 2014, 035007